

18-12-2011

## Satellite evidence for a large source of formic acid from boreal and tropical forests

T Stavrakou

*Belgian Institute for Space Aeronomy*

J F. Muller

*Belgian Institute for Space Aeronomy*

J Peeters

*University of Leuven*

A Razavi

*Universite Libre De Bruxelles*

L Clarisse

*Universite Libre De Bruxelles*

*See next page for additional authors*

Follow this and additional works at: <https://ro.uow.edu.au/scipapers>



Part of the [Life Sciences Commons](#), [Physical Sciences and Mathematics Commons](#), and the [Social and Behavioral Sciences Commons](#)

---

### Recommended Citation

Stavrakou, T; Muller, J F.; Peeters, J; Razavi, A; Clarisse, L; Clerbaux, C; Coheur, P; Hurtmans, D; De Maziere, M; Vigouroux, C; Deutscher, Nicholas; Griffith, David; Jones, Nicholas; and Paton-Walsh, Clare: Satellite evidence for a large source of formic acid from boreal and tropical forests 2011, 26-30.  
<https://ro.uow.edu.au/scipapers/4751>

---

# Satellite evidence for a large source of formic acid from boreal and tropical forests

## Abstract

Formic acid contributes significantly to acid rain in remote environments<sup>1, 2</sup>. Direct sources of formic acid include human activities, biomass burning and plant leaves. Aside from these direct sources, sunlight-induced oxidation of non-methane hydrocarbons (largely of biogenic origin) is probably the largest source<sup>3, 4</sup>. However, model simulations substantially underpredict atmospheric formic acid levels<sup>5, 6, 7</sup>, indicating that not all sources have been included in the models. Here, we use satellite measurements of formic acid concentrations to constrain model simulations of the global formic acid budget. According to our simulations, 100–120 Tg of formic acid is produced annually, which is two to three times more than that estimated from known sources. We show that 90% of the formic acid produced is biogenic in origin, and largely sourced from tropical and boreal forests. We suggest that terpenoids—volatile organic compounds released by plants—are the predominant precursors. Model comparisons with independent observations of formic acid strengthen our conclusions, and provide indirect validation for the satellite measurements. Finally, we show that the larger formic acid emissions have a substantial impact on rainwater acidity, especially over boreal forests in the summer, where formic acid reduces pH by 0.25–0.5.

## Keywords

large, source, formic, acid, boreal, tropical, forests, satellite, evidence

## Disciplines

Life Sciences | Physical Sciences and Mathematics | Social and Behavioral Sciences

## Publication Details

Stavrakou, T., Muller, J. F., Peeters, J., Razavi, A., Clarisse, L., Clerbaux, C., Coheur, P., Hurtmans, D., De Maziere, M., Vigouroux, C., Deutscher, N., Griffith, D., Jones, N. & Paton-Walsh, C. (2012). Satellite evidence for a large source of formic acid from boreal and tropical forests. *Nature Geoscience*, 5 (1), 26-30.

## Authors

T Stavrakou, J F Muller, J Peeters, A Razavi, L Clarisse, C Clerbaux, P Coheur, D Hurtmans, M De Maziere, C Vigouroux, Nicholas Deutscher, David Griffith, Nicholas Jones, and Clare Paton-Walsh

# Satellite Evidence for a Large Source of Formic Acid From Boreal and Tropical Forests

T. Stavrakou<sup>1\*</sup>, J.-F. Müller<sup>1</sup>, J. Peeters<sup>2</sup>, A. Razavi<sup>3</sup>, L. Clarisse<sup>3</sup>, C.  
Clerbaux<sup>4,3</sup>, P.-F. Coheur<sup>3</sup>, D. Hurtmans<sup>3</sup>, M. De Mazière<sup>1</sup>, C. Vigouroux<sup>1</sup>,  
N. M. Deutscher<sup>5,6</sup>, D. W. T. Griffith<sup>5</sup>, N. Jones<sup>5</sup>, C. Paton-Walsh<sup>5</sup>

<sup>1</sup> Belgian Institute for Space Aeronomy, Avenue Circulaire 3, 1180,  
Brussels, Belgium

<sup>2</sup> Department of Chemistry, University of Leuven, B-3001, Heverlee,  
Belgium

<sup>3</sup> Spectroscopie de l'Atmosphère, Service de Chimie Quantique et  
Photophysique, Université Libre de Bruxelles, Belgium

<sup>4</sup> UPMC Univ. Paris 6; Université Versailles St.-Quentin; CNRS/INSU,  
LATMOS-IPSL, Paris, France

<sup>5</sup> School of Chemistry, University of Wollongong, Wollongong, Australia

<sup>6</sup> Institute of Environmental Physics, University of Bremen, Germany

\* E-mail : Trissevgeni.Stavrakou@aeronomie.be

18 Formic acid ( $\text{HCOOH}$ ) has been identified as a major contribu-  
19 tor to acidic rain in remote environments<sup>[1, 2]</sup> but its atmospheric  
20 cycle is far from being understood. Along with direct emissions  
21 by human activities, vegetation fires, and green plants, its major  
22 and most uncertain source is photochemical, and predominantly  
23 biogenic<sup>[3, 4]</sup>. Severe underpredictions of observed formic acid con-  
24 centrations by large scale models in earlier studies<sup>[5, 6, 7]</sup> pointed to  
25 the existence of missing sources. Here we use spaceborne formic  
26 acid column measurements<sup>[8]</sup> as input to an advanced source in-  
27 version algorithm coupled with a global atmospheric model to ob-  
28 tain an improved formic acid global budget. We deduce an annual  
29 formic acid source of 100-120 Tg, i.e. 2-3 times higher than esti-  
30 mated from known sources, with a biogenic contribution of about  
31 90%, mostly from tropical and boreal forests. Model comparisons  
32 with independent formic acid observations strengthen our conclu-  
33 sions and provide indirect validation for the satellite measurements.  
34 The implications of the larger formic acid source on precipitation  
35 acidity are substantial, especially over boreal forests in summer-  
36 time, where the extra biogenic source results in a pH decrease of  
37 0.25-0.5.

38 Known sources of formic acid in the atmosphere include fossil fuel and  
39 biofuel combustion<sup>[9]</sup>, biomass burning<sup>[10]</sup>, plants<sup>[11]</sup>, dry savanna soils<sup>[12]</sup>,  
40 formicine ants<sup>[13]</sup>, cloud processing<sup>[2]</sup>, abiological formation on rock surfaces<sup>[14]</sup>,

41 and photochemical oxidation of volatile organic precursors<sup>[15]</sup>. Among these  
42 sources, the contributions of savanna soils, ants, rocks, and in-cloud forma-  
43 tion are very uncertain, but most probably minor.

44 Based on current inventories, primary formic acid emissions amount to  
45 ca. 10 Tg annually on the global scale (Table 1). The largest contribu-  
46 tion to the global formic acid budget is due to the photo-oxidation of non-  
47 methane hydrocarbons, representing more than 80% of the secondary source  
48 (Table 1). In the base version of the IMAGESv2 global chemistry-transport  
49 model<sup>[16, 17]</sup> used in this work to simulate the formic acid budget, the annual  
50 production from biogenic precursors is estimated at ca. 20 Tg, about twice  
51 lower than in a recent modelling study<sup>[7]</sup>. The major part of this secondary  
52 flux is due to isoprene oxidation by OH (8.9 Tg) and by ozone (3.9 Tg),  
53 followed by monoterpene oxidation (3 Tg). The contribution of isoprene and  
54 monoterpenes is, however, particularly uncertain due to the scarcity of labo-  
55 ratory experiments of HCOOH formation under atmospheric conditions. For  
56 example, the estimated impact of isoprene is largely dependent on the un-  
57 certain fate of key intermediates produced at high yields according to recent  
58 studies, like dihydroxy epoxides from HO<sub>2</sub>-reactions of the isoprene peroxy  
59 radicals<sup>[18]</sup> and hydroperoxy-enones from peroxy isomerisations<sup>[19]</sup>. Formic  
60 acid is removed from the atmosphere through oxidation by OH, accounting  
61 for 27% of the global sink, and dry and wet deposition (cf. Supplementary  
62 Section 3), resulting in a global lifetime of 3-4 days.

63 Global models substantially underpredict the observed HCOOH abun-

dances from available ground-based and aircraft measurements<sup>[5, 6, 7]</sup>, pointing to the existence of missing sources. Their quantitative estimation is, however, very difficult due to the scarcity and limited representativity of these measurements. Recently acquired vertical profiles from two satellite sensors (ACE-FTS and MIPAS)<sup>[20, 21]</sup> are of limited usefulness for probing the emissions, as they sample only the upper troposphere and lower stratosphere.

The new generation IASI/MetOp satellite sensor, launched in 2006, measures in the thermal infrared and has two major advantages compared to its predecessors: high spatial resolution and twice daily global coverage<sup>[22, 23]</sup>. Recently global day-time measurements of formic acid have been obtained and are discussed in detail in Ref.[8]. By limiting the retrieval to clear sky scenes with a large thermal contrast ( $>5\text{K}$ ), the theoretical error on the total column does not exceed 60%, but leads to fewer high-latitude data and to exclusion of oceanic observations. Figure 1 and Supplementary Figures S1, S2 illustrate the IASI-retrieved  $\text{HCOOH}$  monthly column abundances in 2009. The enhanced values observed above the mid and high-latitudes of the Northern Hemisphere during the growing season testify to the existence of a strong source, most likely of biogenic origin, since the biomass burning emission patterns do not generally coincide with enhanced columns (Supplementary Figure S3). Elevated values are also observed in the tropics, above densely vegetated areas. Comparison of the IASI columns with the IMAGESv2 model predictions (Fig. 1) corroborate earlier studies reporting large model underestimations<sup>[5, 6, 7]</sup>.

87 To help interpret this discrepancy, we test the impact of two possible ad-  
 88 ditional sources: (a) the heterogenous oxidation of organic aerosols by OH<sup>[7]</sup>,  
 89 assumed to form one HCOOH molecule per OH lost, and (b) the generation  
 90 of 0.5 HCOOH in the photolysis of hydroperoxy-enones from isoprene<sup>[19]</sup>.  
 91 These hypotheses acknowledge the poor characterisation of organic aerosol  
 92 aging and the large uncertainty associated with the isoprene oxidation mech-  
 93 anism. The global modelled annual organic aerosol source ( $\sim 100$  Tg) ac-  
 94 counts for direct emissions and secondary organic aerosol formation (Sup-  
 95plementary Section 4) and results in an extra global annual HCOOH flux  
 96 of 27 Tg, whereas a larger source (ca. 40 Tg) is issued by the hypothesised  
 97 HCOOH production through the hydroperoxy-enones (Supplementary Sec-  
 98tion 2). Although both scenarios lead to significant enhancements in the  
 99 HCOOH columns allowing for some improvement in the model predictions,  
 100 especially in tropical regions like Indonesia and Amazonia, they prove inad-  
 101 equate to reconcile the model with the high observed columns in mid and  
 102 high-latitude areas (Fig. 1, Supplementary Figure S4), underscoring the need  
 103 for an even larger HCOOH source.

104 To properly quantify the formic acid source required to reproduce the  
 105 space-based constraints we use the adjoint source inversion method to infer  
 106 “top-down” emissions at the resolution of the global model<sup>[24]</sup> (cf. Methods).  
 107 Two optimisation experiments are designed and performed, both constrained  
 108 by monthly IASI columns. Along with the vegetation fire source, we opti-  
 109mise either a direct HCOOH emission from vegetation (Opt1), or, a secondary

110 HCOOH source from the OH-oxidation of an as-yet-unidentified biogenic pre-  
111 cursor, with a global lifetime taken equal to about one day (Opt2, Table 1).  
112 These simple settings are meant to represent situations in which the missing  
113 HCOOH source is due to direct emission or photochemical formation on very  
114 short time frames, or through a collection of compounds leading to HCOOH  
115 formation after a number of unspecified intermediate steps.

116 Both optimisations predict the existence of a substantial biogenic source  
117 of HCOOH estimated at about 90-110 Tg annually, i.e. 3.5 times larger than  
118 in the a priori budget, as illustrated in Table 1. This brings the contribu-  
119 tion of biogenic sources to 90% of the global HCOOH budget, the remainder  
120 being due to fires and human activities. The optimisation improves signifi-  
121 cantly the agreement between the model and IASI columns in terms of both  
122 column amplitude and seasonality, also at high northern latitudes where the  
123 differences were more pronounced, as shown by comparisons in Fig. 1, Supple-  
124 mentary Figures S1-S2 and Table S1. The extra emission over boreal forests  
125 is presumably largely due to oxidation of biogenic volatile compounds from  
126 coniferous trees, for which HCOOH formation pathways remain so far unex-  
127 plored. A large contribution of primary biogenic HCOOH emissions cannot  
128 be excluded, but appears less likely, since high emissions of HCOOH from  
129 plants are not corroborated by reported flux measurements<sup>[25, 26]</sup>.

130 The extra secondary HCOOH source inferred from the Opt2 inversion is  
131 estimated at 65 Tg annually, of which tropical ecosystems (30 S-30 N) and  
132 extratropical latitudes (30-90 N) contribute 40 Tg and 24 Tg annually, re-



133 spectively. The strong contribution of boreal forests seen in its geographical  
134 distribution (Fig. 3) clearly suggests that oxidation of terpenoids emitted by  
135 these forests generates substantial amounts of HCOOH. The seasonal varia-  
136 tion of the extra source displays a summertime maximum at high latitudes,  
137 which is however less pronounced than in isoprene and terpene emission in-  
138 ventories used in global models (Supplementary Figure S5). Interestingly,  
139 relatively high emissions are derived also during spring at these latitudes,  
140 possibly reflecting higher base emission rates in spring (compared to summer  
141 and autumn), as found in recent field studies of monoterpene emissions<sup>[27]</sup>. In  
142 the tropics the HCOOH precursor emission is largest at the end of the dry sea-  
143 son, but is weakly correlated with the vegetation fire source, which is however  
144 of low magnitude. Note that, should the entire missing source of HCOOH  
145 be attributed to monoterpenes only, a total molar yield of 200% HCOOH  
146 in the oxidation of monoterpenes would be required; however, the contribu-  
147 tion of terpenoid compounds other than isoprene and monoterpenes might be  
148 substantial, since field measurements over boreal forests have suggested the  
149 existence of large emissions of undetected short-lived organic compounds<sup>[28]</sup>.

150 Both the magnitude and distribution of the source inferred from IASI  
151 are found to be only weakly sensitive to model uncertainties as shown by  
152 the results of sensitivity studies detailed in Supplementary Section 8. In  
153 particular, we investigated the influence of uncertainties in the wet and dry  
154 deposition parameterisations, the chemical scheme, and the assumed errors  
155 on the spaceborne data. In most cases, the deduced annual global biogenic

156 source is found to differ by less than 10% from the reference case, confirming  
157 the robustness of the inferred estimates.

158 In an attempt to evaluate the IASI-derived source, we have conducted ex-  
159 tensive comparisons of the model with independent HCOOH measurements  
160 (Supplementary Section 5). Comparisons with infrared column measure-  
161 ments (FTIR) at Wollongong and Reunion Island show substantial improve-  
162 ments after optimisation, as seen from the average bias reduction by a factor  
163 of 3 or more at both locations (Fig. 2). At ground level, the a priori model  
164 underprediction of HCOOH concentration measurements in air and precip-  
165 itation by large factors gives way to an a posteriori mean underestimation  
166 by a factor of about two or less in all regions (Supplementary Figure S6-S7).  
167 More precisely, the average gas-phase (liquid) concentration is increased from  
168 0.29 ppbv ( $1.32 \mu\text{mol/L}$ ) in the a priori simulation to 0.78-1.17 ppbv ( $4.0$ -  
169  $4.2 \mu\text{mol/L}$ ) in the optimisation runs, to be compared to the observed 1.33  
170 ppbv ( $6.7 \mu\text{mol/L}$ ). Consistent with these results, the optimisation brings  
171 also the model significantly closer to airborne concentration measurements  
172 above North America and the Pacific (Supplementary Figure S8). Over-  
173 all, these comparisons lend confidence to the IASI dataset, and therefore to  
174 the strong biogenic source inferred from the optimisation. The comparisons,  
175 however, also point to a limited ability of the model to capture the observed  
176 variability and vertical profile. Although this is largely due to the limited  
177 representativity of local measurements, it might also reflect the existence of  
178 important shortcomings in the representation of the formic acid sources and

179 sinks.

180 We quantify the global impact of the IASI-constrained HCOOH source  
181 on precipitation acidity using the calculated wet deposition fluxes of nitrate,  
182 sulphate, ammonium, formate and acetate ions (Supplementary Section 7).  
183 The inferred decrease in pH due to the additional HCOOH source is es-  
184 timated at 0.25-0.5 over boreal forests in summertime, and 0.15-0.4 above  
185 tropical vegetated areas throughout the year (Supplementary Figure S9).  
186 Our model simulations predict that formic acid alone accounts for as much  
187 as 60-80% of the rainwater acidity over Amazonia, in accordance with in  
188 situ measurements<sup>[29]</sup>, but also over boreal forests during summertime. Its  
189 contribution is also substantial at mid-latitudes, in particular over much of  
190 the US, where it reaches 30-50% during the summer (Supplementary Fig-  
191 ure S10). Given the remaining underestimation of a posteriori modelled  
192 HCOOH concentrations against independent measurements (Supplementary  
193 Table S5), the large calculated impacts on precipitation acidity are probably  
194 conservative estimates. They underscore the importance of HCOOH in acid  
195 deposition in different environments, although its consequences for ecosys-  
196 tems are likely limited due to the assimilation of simple carboxylic acids by  
197 the biota<sup>[30]</sup>.

198 In this letter we have revisited the formic acid global distribution and  
199 budget, using source inversion constrained by space observations. We found  
200 a biogenic source of formic acid of the order of 100 Tg annually, much larger  
201 than the current state-of-the-art estimates. A large fraction of this source

202 originates in boreal and tropical forests, and although it remains mostly  
203 unidentified, it is likely to be of secondary origin. These findings suggest that  
204 formic acid is a high-yield product in the oxidation of organic compounds  
205 emitted abundantly by plant ecosystems, such as monoterpenes and other  
206 terpenoids, and underscore the need for further research on the emissions  
207 and chemistry of biogenic precursors.

## 208 **Methods**

### 209 **Modelling**

210 The simulations are performed with the IMAGESv2 global chemistry  
211 transport model for the year 2009, after a four-month spin-up time. The  
212 model resolution is  $4^\circ \times 5^\circ$  with 40 vertical levels. The accompanying Sup-  
213plementary material includes : details on HCOOH sources and sinks used in  
214 the base model (Sections 1-3), a description of the organic aerosol module  
215 (Section 4), a description of ground-based and aircraft measurements used  
216 for validation purposes and comparisons with the model predictions (Section  
217 5), discussion on the uncertainties of the IASI columns (Section 6), on the  
218 impact of formic acid sources on precipitation acidity (Section 7), and on  
219 the conducted sensitivity inversions (Section 8). Results are illustrated in  
220 Supplementary Figures S1-S12 and Tables S1-S7.

### 221 **Method for source inversion**

222 The source inversion is realised through minimisation of the cost function

223  $J$ , which measures the misfit between the model and the observations. By  
 224 using the adjoint model method, the derivatives of the cost function  $J$  are  
 225 computed with respect to a number of control variables  $\mathbf{f}$  (emission param-  
 226 eters)

$$J(\mathbf{f}) = \frac{1}{2}[(H(\mathbf{f}) - \mathbf{y})^T \mathbf{E}^{-1}(H(\mathbf{f}) - \mathbf{y}) + \mathbf{f}^T \mathbf{B}^{-1} \mathbf{f}], \quad (1)$$

227 where  $H(\mathbf{f})$  is the model operator acting on the control variables,  $\mathbf{y}$  is the  
 228 observation vector,  $\mathbf{E}$ ,  $\mathbf{B}$  are the covariance matrices of the errors on the  
 229 observations and the emission parameters  $\mathbf{f}$ , respectively, and  $^T$  is the trans-  
 230 pose. The method makes use of a priori distributions for biogenic and pyro-  
 231 genic emissions, obtained from available inventories (Supplementary Section  
 232 1). The adjoint method enables handling of problems with large numbers  
 233 of control variables, e.g. emission inversions at the model resolution. The  
 234 cost function is minimised through an iterative descent algorithm which uses  
 235 the forward and the adjoint model of IMAGESv2. About 50 iterations are  
 236 usually needed to reach the minimum and derive the “top-down” emission es-  
 237 timates. The norm of the gradient of the cost function is reduced by a factor  
 238  $\geq 1000$  after optimisation. In both optimisations, the pyrogenic and biogenic  
 239 emission source strengths are updated (ca. 12,000 emission parameters). The  
 240 errors on the emission parameters, i.e. the square roots of the diagonal el-  
 241 ements of  $\mathbf{B}$ , are assumed to be a factor of two for biogenic emissions, and  
 242 a factor of 2.5 for biomass burning, whereas spatiotemporal correlations are  
 243 introduced through the off-diagonal elements<sup>[24]</sup>. The matrix  $\mathbf{E}$  is assumed

244 diagonal. The errors on IASI columns are taken as the quadratic sum of a  
245 30% relative error and a  $4 \times 10^{15}$  molec.cm<sup>-2</sup> absolute error. This estimate  
246 does not account for a possible bias in the IASI measured columns. The  
247 latter could not be quantified due to the lack of correlative measurements.  
248 At Wollongong, however, we find IASI columns to be biased 30% low as  
249 compared to FTIR ground-based measurements in 2008-2009, with a high  
250 degree of correlation (0.84, Supplementary Section 6). Note also that the  
251 model inversions do not account for the heterogeneous vertical sensitivity of  
252 IASI. The application of a vertical smoothing to the model columns could  
253 potentially decrease the global HCOOH source by ca. 10%.

## References

- [1] Galloway, J. N., Likens, G. E., Keene, W. C. & Miller, J. M. The composition of precipitation in remote areas of the world. *J. Geophys. Res.* **87**, 8771–8786 (1982).
- [2] Chameides, W. L. & Davis, D. D. Aqueous-phase source of formic acid in clouds. *Nature* **304**, 427–429 (1983).
- [3] Kavouras, I. G., Mihalopoulos, N. & Stephanou, E. G. Formation of atmospheric particles from organic acids produced by forests. *Nature* **395**, 683–686 (1998).
- [4] Glasius, M. Sources to formic acid studied by carbon isotopic analysis and air mass characterization. *Atmos. Environ.* **34**, 2471–2479 (2000).
- [5] von Kuhlmann, R., Lawrence, M. G., Crutzen, P. J. & Rasch, P. J. A model for studies of tropospheric ozone and non-methane hydrocarbons: Model evaluation of ozone related species. *J. Geophys. Res.* **108**(D23), 4729, doi:10.1029/2002JD003348 (2003).
- [6] Ito, A., Sillman, S. & Penner, J. E. Effects of additional nonmethane volatile organic compounds, organic nitrates, and direct emissions of oxygenated organic species on global tropospheric chemistry. *J. Geophys. Res.* **112**, D06309, doi:10.1029/2005JD006556 (2007).

- 273 [7] Paulot, F. *et al.* Importance of secondary sources in the atmospheric  
274 budgets of formic and acetic acids. *Atmos. Chem. Phys.* **11**, 1989–2013  
275 (2011).
- 276 [8] Razavi, A. *et al.* Global distributions of methanol and formic acid re-  
277 trieved for the first time from the IASI/MetOp thermal infrared sounder.  
278 *Atmos. Chem. Phys.* **11**, 857–872 (2011).
- 279 [9] Kawamura, K., Ng., L. L. & Kaplan, I. R. Determination of organic acids  
280 (C<sub>1</sub>–C<sub>10</sub>) in the atmosphere, motor exhausts and engine oils. *Environ. Sci.*  
281 *Tech.* **19**, 1082–1086 (1985).
- 282 [10] Andreae, M. O. & Merlet, P. Emission of trace gases and aerosols from  
283 biomass burning. *Global Biogeochem. Cy.* **15**, 955–966 (2001).
- 284 [11] Gabriel R., Schäfer, L., Gerlach, C., Rausch, T. & Kesselmeier, J. Fac-  
285 tors controlling the emissions of volatile organic acids from leaves of *Quer-*  
286 *cus ilex* L. (Holm oak). *Atmos. Environ.* **33**, 1347–1355 (1999).
- 287 [12] Sanhueza, E. & Andreae, M. O. Emissions of formic and acetic acids  
288 from tropical savanna soils. *Geophys. Res. Lett.* **18**(9), 1707–1710 (1991).
- 289 [13] Graedel, T. E. & Eisner, T. Atmospheric formic acid from formicine  
290 ants: a preliminary assessment. *Tellus B* **40**, 335–339 (1988).
- 291 [14] Ohta, K., Ogawa, H. & Mizuno, T. Abiological formation of formic acid  
292 on rocks in nature. *Appl. Geochem.* **15**, 91–95 (2000).



- 293 [15] Neeb, P., Sauer, F., Horie, O. & Moortgat, G. R. Formation of hydrox-  
 294 ymethyl hydroperoxide and formic acid in alkene ozonolysis in the presence  
 295 of water vapor. *Atmos. Environ.* **31**, 1417–1423 (1997).
- 296 [16] Müller, J.-F. & Stavrakou, T. Inversion of CO and NOx emissions using  
 297 the adjoint of the IMAGES model. *Atmos. Chem. Phys.* **5**, 1157–1186  
 298 (2005).
- 299 [17] Stavrakou, T. *et al.* Evaluating the performance of pyrogenic and bio-  
 300 genic emission inventories against one decade of space-based formaldehyde  
 301 columns. *Atmos. Chem. Phys.* **9**, 1037–1060 (2009).
- 302 [18] Paulot, F. *et al.* Unexpected epoxide formation in the gas-phase pho-  
 303 tooxidation of isoprene. *Science* **325**, 730–733 (2009).
- 304 [19] Peeters, J. & Müller, J.-F. HOx radical regeneration in isoprene oxi-  
 305 dation via peroxy radical isomerisations, II: Experimental evidence and  
 306 global impact. *Phys. Chem. Chem. Phys.* **12(42)**, 14,227–14,235 (2010).
- 307 [20] González Abad, G. *et al.* Global distribution of upper tropospheric  
 308 formic acid from the ACE-FTS. *Atmos. Chem. Phys.* **9**, 8039–8047 (2009).
- 309 [21] Grutter, M. *et al.* Global distribution and variability of formic acid  
 310 as observed by MIPAS-ENVISAT. *J. Geophys. Res.* **115**, D10303,  
 311 doi:10.1029/2009JD012980 (2010).

- 312 [22] Clerbaux, C. *et al.* Monitoring of atmospheric composition using the  
313 thermal infrared IASI/MetOp sounder. *Atmos. Chem. Phys.* **9**, 6041–6054  
314 (2009).
- 315 [23] Clarisse, L., Clerbaux, C. Dentener, F. Hurtmans, D. & Coheur, P. F.  
316 Global ammonia distribution derived from infrared satellite observations.  
317 *Nature Geoscience* **2**, 479–483 (2009).
- 318 [24] Stavrakou, T. *et al.* First space-based derivation of the global atmo-  
319 spheric methanol emission fluxes. *Atmos. Chem. Phys.* **11**, 4873–4898  
320 (2011).
- 321 [25] Kuhn, U. *et al.* Exchange of short-chain monocarboxylic acids by vege-  
322 tation at a remote tropical forest site in Amazonia. *J. Geophys. Res.* **107**,  
323 D20, doi:10.1029/2000JD000303 (2002).
- 324 [26] Kesselmeier, J., Bode, K., Gerlach, C. & Jork, E. M. Exchange of at-  
325 mospheric formic and acetic acids with trees and crop plants under con-  
326 trolled chamber and purified air conditions. *Atmos. Environ.* **32**, 1765–  
327 1775 (1998).
- 328 [27] Holzinger, R., Lee, A., McKay, M. & Goldstein, A. H. Seasonal vari-  
329 ability of monoterpene emission factors for a Ponderosa pine plantation in  
330 California. *Atmos. Chem. Phys.* **6**, 1267–1274 (2006).
- 331 [28] Di Carlo, P. *et al.* Missing OH reactivity in a forest: evidence for un-  
332 known reactive biogenic VOCs. *Science* **304**, 722–725 (2004).

- 333 [29] Andreae, M. O., Talbot, R. W., Andreae, T. W. & Harriss, R. C. Formic  
334 and Acetic Acid Over the Central Amazon Region, Brazil 1. Dry Season.  
335 *J. Geophys. Res.* **93(D2)**, 1616–1624 (1988).
- 336 [30] Keene, W. C. & Galloway, J. N. Organic acidity in precipitation of North  
337 America. *Atmos. Environ.* **18**, 2491–2497 (1984).

### **Additional information**

Correspondence and requests for materials should be addressed to T. S.

### **Acknowledgements**

This study has been supported by the projects PRODEX A3C of the European Space Agency funded by the Belgian Science Policy Office, and the IBOOT, BIOSOA, AGACC and AGACC-II projects within the “Science for a Sustainable Development” research programme funded by the Belgian Science Policy Office. Financial support by the “Actions de Recherche Concertées” (Communauté Française de Belgique) is also acknowledged. IASI has been developed and built under the responsibility of the Centre National d’Etudes Spatiales (CNES, France). It is flown onboard the Metop satellites as part of the EUMETSAT Polar System. The IASI L1 data are received through the EUMETCast near real time data distribution service. L.C. and P.-F.C. are respectively Postdoctoral Researcher and Research Associate with F.R.S.-FNRS. The Australian Research Council (Grant DP110101948) is gratefully acknowledged for their funding of the Wollongong HCOOH measurements. C.V. and M.D.M. are grateful to the BIRA and LACY team members who support the FTIR observations at Reunion Island.

### **Author contributions**

T.S. and J.-F.M. obtained the results, drafted the manuscript and prepared the figures. J.P. developed the isoprene degradation mechanism used to estimate the photochemical source of formic acid in the model. A.R.,

360 L.C., P.-F.C., D.H. and C.C. carried out the first retrievals of formic acid  
361 observations from space. C.C. contributed also actively in the development  
362 of the IASI sensor. C.V. and M.D.M. retrieved the FTIR data at Reunion  
363 Island. N.D., D.G., N.J. and C.P.-W. retrieved the FTIR observations at  
364 Wollongong.

### 365 **Competing Financial Interests Statement**

366 The authors declare no competing financial interests as defined by the Na-  
367 ture Publishing Group or other interests that might be perceived to influence  
368 the results and discussion reported in this paper.



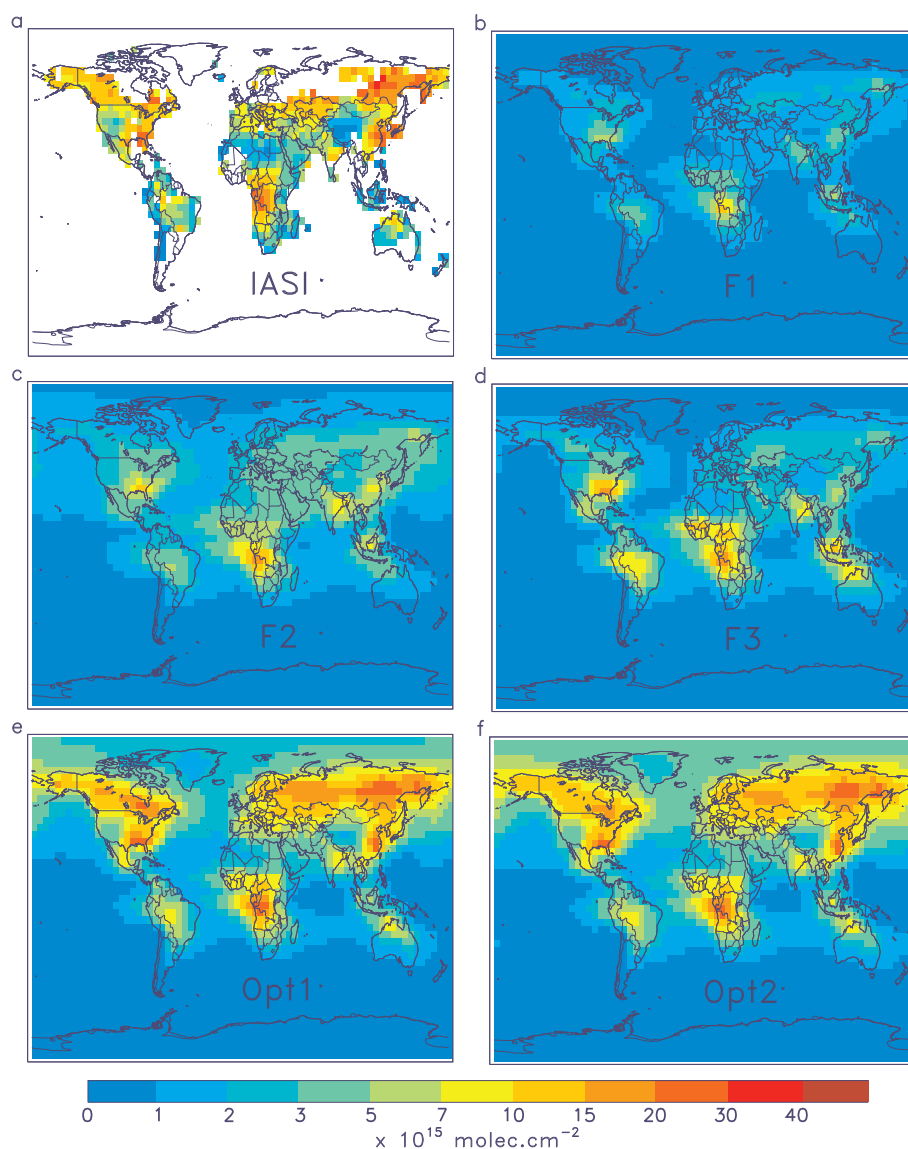


Figure 1: **Monthly averaged HCOOH columns in June 2009 (expressed in  $10^{15} \text{ molec.cm}^{-2}$ ).** **a**, Observed by IASI. **b**, Simulated by the standard model (F1, Table 1). **c**, Simulated assuming that HCOOH is produced in the heterogeneous oxidation of organic aerosols by OH (F2). **d**, Simulated accounting for a production of HCOOH in the photolysis of hydroperoxy-enones from isoprene (F3). **e-f**, Inferred from source inversion assuming either a primary (Opt1) or a secondary (Opt2) biogenic HCOOH source (Table 1).

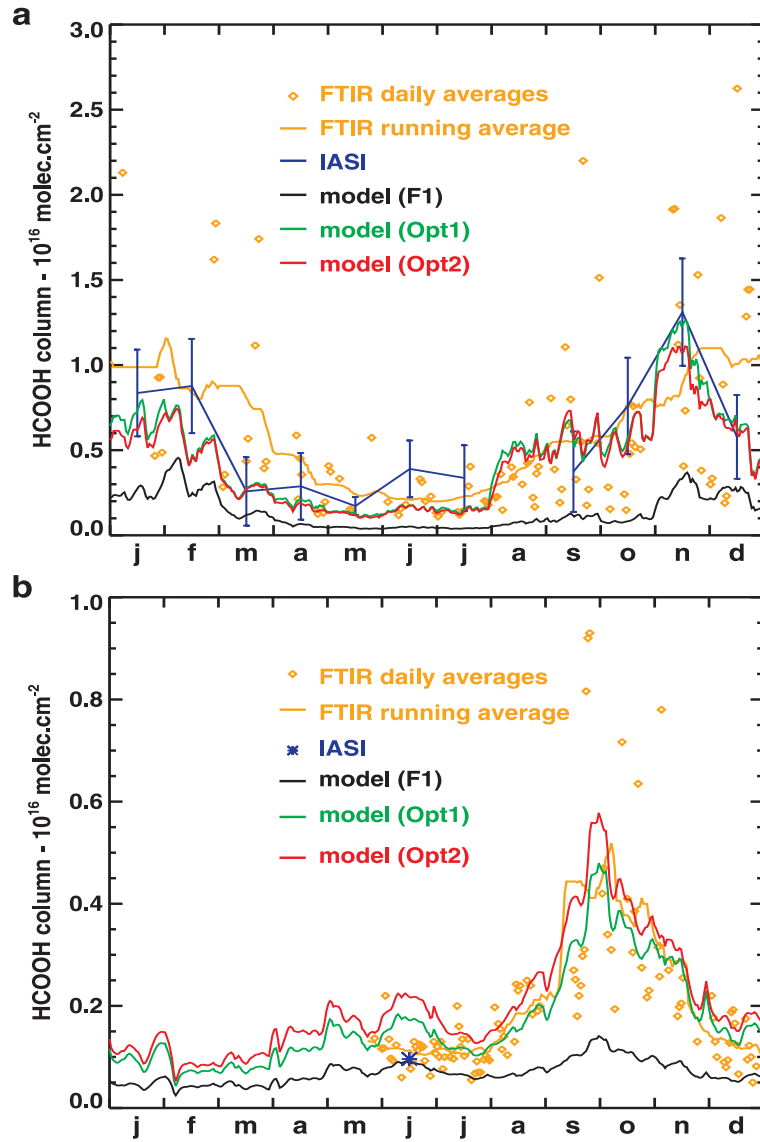


Figure 2: **Comparisons between FTIR, IASI and modelled HCOOH columns in 2009.** **a**, Daily and 30-day running FTIR column averages at Wollongong (34.41 S, 150.88 E) (orange) and model results from the standard simulation F1 (black) and the two inversions Opt1 (green) and Opt2 (red). Average IASI columns within a radius of 4 degrees around the site and their standard deviations are shown in blue. **b**, Same for Reunion Island (21 S, 55 E). Except for June, IASI columns are not available at this site due to the thermal contrast requirement for their retrieval.



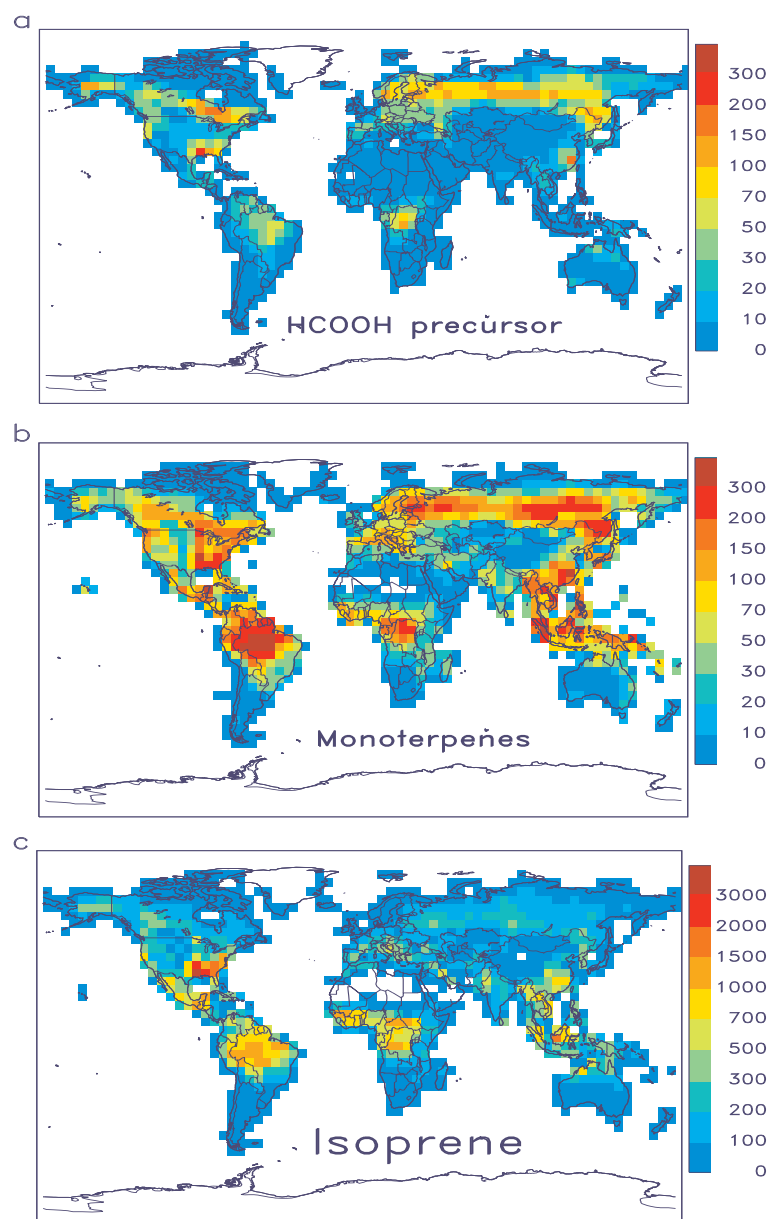


Figure 3: **Global distribution of biogenic emissions in  $\mu\text{g C m}^{-2} \text{s}^{-1}$  in July 2009.** **a**, HCOOH precursor as deduced from the Opt2 inversion (Table 1). **b-c**, Monoterpene and isoprene emissions from MEGAN inventory, cf. Supplementary Section 1.

Table 1: Description of the simulations and inversions performed in this study, and global HCOOH budget calculated with IMAGESv2 and comparison with previous work. Notes : (a) includes biofuel burning and cattle emissions, (b) includes a soil source of  $1.8 \text{ Tg yr}^{-1}$ , (c) of which  $19.3 \text{ Tg yr}^{-1}$  is due to known sources and  $64.7 \text{ Tg yr}^{-1}$  to unidentified precursors, (d) A priori budget, but an estimated extra source of  $2 \text{ Tmol yr}^{-1}$  is invoked to reconcile the model with HCOOH observations, (e) includes a dust sink of  $1.38 \text{ Tg yr}^{-1}$ .

F1	standard simulation					
F2	including a production of HCOOH in the heterogeneous oxidation of organic aerosols (OA) by OH					
F3	including a production of HCOOH in the photolysis of hydroperoxy-enones from isoprene					
Inversion - Opt1	derive a primary HCOOH biogenic source using IASI					
Inversion - Opt2	derive a secondary HCOOH biogenic source using IASI					
<i>Sources (Tg/yr)</i>	F1	F2	F3	Opt1	Opt2	Paulot et al. 2011
Anthropogenic	4	4	4	4	4	$2.28^a$
Pyrogenic	2.9	2.9	2.9	4	4	1.5
Biogenic primary	5.6	5.6	5.6	88	5.6	$4.37^b$
Photochemical						
Biogenic	19.3	19.3	58.3	19.3	$84^c$	42.2
Anthrop./pyrog.	4.2	4.2	4.2	4.6	4.6	6.35
OA+OH	0	27	0	0	0	(15)
<b>Total</b>	<b>36</b>	<b>63</b>	<b>75</b>	<b>120</b>	<b>102</b>	<b><math>56.7^d</math></b>
<i>Sinks (Tg/yr)</i>						
OH oxidation	9.6	19	20	27	28.4	10.6
Dry deposition	12.7	19.9	26.8	49.5	33.6	$26.0^e$
Wet deposition	13.7	24.1	28.2	43.4	40	20.1
Lifetime (days)	4	4.5	3.8	3.5	4.3	3.2

## Supplementary Information for

# Satellite Evidence for a Large Source of Formic Acid From Boreal and Tropical Forests

T. Stavrakou<sup>1\*</sup>, J.-F. Müller<sup>1</sup>, J. Peeters<sup>2</sup>, A. Razavi<sup>3</sup>, L. Clarisse<sup>3</sup>, C. Clerbaux<sup>4,3</sup>, P.-F. Coheur<sup>3</sup>, D. Hurtmans<sup>3</sup>, M. De Mazière<sup>1</sup>, C. Vigouroux<sup>1</sup>, N. M. Deutscher<sup>5,6</sup>, D. W. T. Griffith<sup>5</sup>, N. Jones<sup>5</sup>, C. Paton-Walsh<sup>5</sup>

<sup>1</sup> Belgian Institute for Space Aeronomy, Avenue Circulaire 3, 1180, Brussels, Belgium

<sup>2</sup> Department of Chemistry, University of Leuven, B-3001, Heverlee, Belgium

<sup>3</sup> Spectroscopie de l'Atmosphère, Service de Chimie Quantique et Photophysique, Université Libre de Bruxelles, Belgium

<sup>4</sup> UPMC Univ. Paris 6; Université Versailles St.-Quentin; CNRS/INSU, LATMOS-IPSL, Paris, France

<sup>5</sup> School of Chemistry, University of Wollongong, Wollongong, Australia

<sup>6</sup> Institute of Environmental Physics, University of Bremen, Germany

\* E-mail : Trissevgeni.Stavrakou@aeronomie.be

## Contents

<b>1 Emissions of Formic Acid in the IMAGESv2 global CTM</b>	<b>2</b>
<b>2 Photochemical Sources of Formic Acid</b>	<b>2</b>
2.1 Isoprene oxidation by OH . . . . .	2
2.2 Ozonolysis of alkenes . . . . .	5
2.3 Oxidation of monoterpenes . . . . .	7
<b>3 Sinks of Formic Acid</b>	<b>7</b>
<b>4 Organic Aerosol Modeling in IMAGESv2</b>	<b>8</b>
<b>5 Ground-based and Aircraft Measurements</b>	<b>9</b>
<b>6 Uncertainties on IASI HCOOH columns</b>	<b>10</b>
<b>7 Impact on Precipitation Acidity</b>	<b>11</b>
<b>8 Sensitivity Inversions</b>	<b>11</b>
<b>9 Tables</b>	<b>14</b>
<b>10 Figures</b>	<b>20</b>
<b>References</b>	<b>32</b>

# 1 Emissions of Formic Acid in the IMAGESv2 global CTM

The IMAGESv2 global chemistry-transport model is run at  $4^\circ \times 5^\circ$  resolution and is resolved at 40 vertical levels from the surface up to the lower stratosphere. The model meteorology is provided by ERA-Interim analyses of the ECMWF data center. The model has been extensively described in previous work [S1, S2, S3, S4], except for the model updates detailed in this Supplement. The model simulations are performed for year 2009, after a four-month spin-up time starting on September 1, 2008.

Global fossil fuel and biofuel NMVOC emissions are obtained from the RETRO[S5] database for the year 2000, which is overwritten by the 2009 REAS[S6] inventory over Asia. The global annual anthropogenic source of formic acid (including biofuel use) amounts to  $2.2 \text{ Tg yr}^{-1}$ , when the contribution of HCOOH to the carboxylic acids emissions in these inventories is assumed to be 25%. Formic acid emissions from cattle are estimated at  $1.8 \text{ Tg yr}^{-1}$ [S7]. The emissions of the main biogenic precursors of formic acid, isoprene and the monoterpenes, are both obtained from inventories based on the MEGAN model[S8]. The global annual sources of isoprene and monoterpenes in 2009 amount to 424 Tg and 97 Tg, respectively.

Vegetation fire emissions are obtained from the latest version of the Global Fire Emission Database[S9], by applying updated (in 2007) emission factors[S10]. For HCOOH, the emission factors are 1.13, 2.43 and 0.63 g HCOOH/kg of dry matter for tropical, extratropical, and savanna burning, respectively, and the global biomass burning flux is estimated at 2.9 Tg for the year 2009. Monthly HCOOH biomass burning emissions between May and August 2009 are shown in Fig. S3. Monthly emissions of HCOOH from leaves are the average of the fluxes estimated between 1983 and 1995 by the ORCHIDEE global dynamic vegetation model[S11], and amount at  $5.6 \text{ Tg yr}^{-1}$ .

## 2 Photochemical Sources of Formic Acid

This section deals with the photochemical HCOOH formation in the standard (F1, Table 1) version of IMAGESv2.

### 2.1 Isoprene oxidation by OH

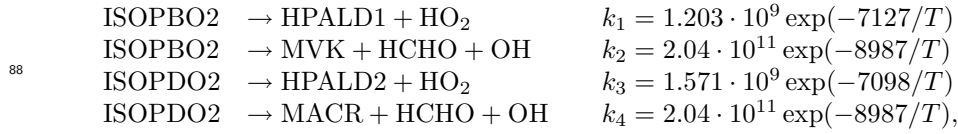
The OH-initiated isoprene oxidation mechanism in IMAGESv2 is based on the new theoretically-based LIM0 mechanism[S12, S13], which has been implemented in IMAGESv2 and evaluated against aircraft observations[S4]. This scheme puts forward that isomerisation reactions of specific isomer/conformer peroxy radicals from isoprene lead to the formation of HOx radicals and photolabile hydroperoxy-enones, most likely hydroperoxy methylbutenals (HPALDs) at rates faster than those of traditional reactions of the isoprene peroxy radicals

71 with NO and HO<sub>2</sub> in most remote atmospheric regimes, offering thereby a likely  
 72 explanation for the high abundances of HOx radicals observed in isoprene-rich  
 73 areas<sup>[S14, S15]</sup>. Unfortunately, the rates of key isomerisation reactions in LIM0  
 74 remain uncertain, in particular the 1,6-H shift of the  $\delta$ -hydroxy peroxy radi-  
 75 cals leading to the formation of the HPALDs. Based on the results of isoprene  
 76 oxidation experiments conducted at low NOx levels<sup>[S16]</sup>, the theoretical best  
 77 estimate for these rates appeared to be likely overestimated by a factor of 2 or  
 78 3<sup>[S13, S17]</sup>. However, even such a rate reduction has only limited consequences  
 79 on the yields of the primary products, due to the strongly non-linear dependence  
 80 of the yields on the 1,6-H shift rates<sup>[S13, S4]</sup>.

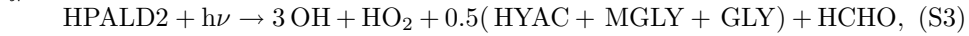
81 In IMAGESv2 the reaction of isoprene with OH is written as



82 where ISOPBO2, ISOPDO2 are the peroxy radicals formed through OH addition to  
 83 the terminal carbons, and ISOPEO2 represent the peroxy radicals formed through ad-  
 84 dition to the inner carbons. The  $\delta$ -hydroxy peroxy radicals are not explicitly  
 85 included, since their traditional reaction products have negligible yields accord-  
 86 ing to LIM0 in most atmospheric conditions. The isomerisation of the isoprene  
 87 hydroxyperoxy radicals is accounted through the reactions :



89 where  $T$  is the temperature (in K) and MVK, MACR denote methylvinylketone  
 90 and methacrolein, respectively. The adopted rates  $k_1$ – $k_4$  (in s<sup>-1</sup>) account for a  
 91 factor of 2 reduction of the theoretical best estimates for the 1,6-H shift rates of  
 92 the  $\delta$ -hydroxy peroxy radicals<sup>[S4]</sup>. Photolysis is believed to be the main sink re-  
 93 action of the HPALDs accounting for about two thirds of the global sink<sup>[S4]</sup>, and  
 94 leading to the regeneration of one or several OH radicals. However, the further  
 95 oxidation of the photolysis products remains to be elucidated. In the current  
 96 version of the mechanism<sup>[S4]</sup>, the photolysis of the HPALDs is represented as



98 where GLY, MGLY, HYAC, and GLYALD are abbreviations for glyoxal, methyl-  
 99 glyoxal, hydroxyacetone and glycolaldehyde, respectively. The possibility that  
 100 HPALD oxidation leads to additional HCOOH formation is explored in the F3  
 101 simulation (Table 1).

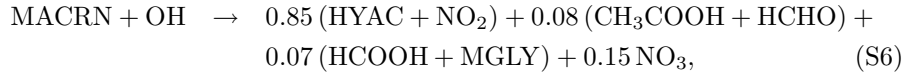
102 A yield of 6% of isoprene nitrates (ISOPN) is assumed in the reaction of  
 103 isoprene peroxy radicals with NO. Their oxidation by OH leads to HCOOH  
 104 formation<sup>[S18]</sup>, as summarised below :



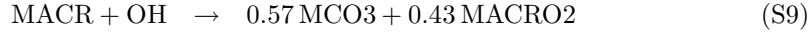
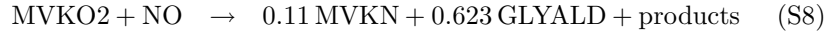
105



106



107 where MVKN and MACRN are nitrates produced in the oxidation of MVK and  
108 MACR by OH :



109 The oxidation by OH of isoprene hydroxy-hydroperoxides issued by the reac-  
110 tion of isoprene peroxy radicals with HO<sub>2</sub> leads to the formation of epoxides<sup>[S16]</sup>  
111 (IEPOX) :



112 Their further oxidation by OH is assumed<sup>[S16]</sup> to lead to (among others) HCOOH  
113 and GLYALD :

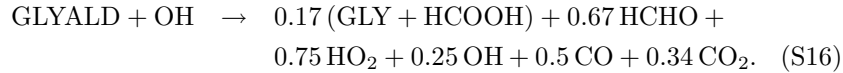


114



115 Note however that HCOOH is not produced from IEPOX according to the  
116 protocol rules of the Master Chemical Mechanism<sup>[S17]</sup>.

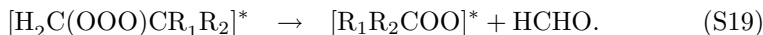
117 According to a laboratory study of the Orléans group<sup>[S19]</sup>, the oxidation of  
118 GLYALD is also a source of HCOOH :



119 Glycolaldehyde is mainly produced from the oxidation of MVK, ISOPN, IEPOX  
 120 and the HPALDs (see above). It is also a major product in the oxidation  
 121 of ethylene by OH<sup>[S20]</sup>. Another laboratory study by the Orléans group<sup>[S21]</sup>  
 122 proposed that HCOOH is formed in the OH-oxidation of hydroxyacetone, a  
 123 major secondary product in the oxidation of isoprene; however, the proposed  
 124 formation mechanism appears rather unusual. More recent experiments<sup>[S22]</sup>  
 125 give evidence that this production does not occur at atmospheric conditions,  
 126 and hence is not accounted in this study.

## 127 2.2 Ozonolysis of alkenes

128 The ozonolysis of alkenes proceeds via the addition of O<sub>3</sub> to the C=C bond to  
 129 form a primary ozonide which rapidly decomposes to one or two sets of Criegee  
 130 intermediate (CI) plus a carbonyl<sup>[S23, S24]</sup>. In the case of terminal alkenes  
 131 (H<sub>2</sub>C=CR<sub>1</sub>R<sub>2</sub>), ozonolysis forms the smallest CI, [H<sub>2</sub>COO]\* :



133 Due to the high exothermicity of the overall reaction (S17-S19), both products  
 134 are chemically activated and only a fraction of the energy-rich CIs becomes  
 135 collisionally stabilised, while the rest undergoes various “prompt” unimolecular  
 136 reactions. This stabilised fraction is close to 0.37 (average of 5 experimental  
 137 studies)<sup>[S25]</sup> for [H<sub>2</sub>COO]\* originating from C<sub>2</sub>H<sub>4</sub> + O<sub>3</sub>. Larger values are  
 138 expected in the case of higher alkenes, for which a larger fraction of the energy  
 139 will be partitioned to the larger fragment R<sub>1</sub>C(O)R<sub>2</sub>. Nevertheless, we adopt  
 140 here the value of 0.37 for the cases of C<sub>3</sub>H<sub>6</sub>, MACR and MVK.

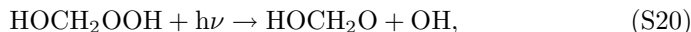
141 In tropospheric conditions, reaction of the stabilised Criegee intermediates  
 142 (SCIs) with H<sub>2</sub>O is generally by far the dominant sink of the SCIs. Laboratory  
 143 experiments<sup>[S24, S26, S27, S28, S29]</sup> of alkene ozonolysis indicate that the reac-  
 144 tion of H<sub>2</sub>COO with H<sub>2</sub>O forms formic acid and hydroxymethyl hydroperoxide  
 145 (HMHP). It has been shown<sup>[S24, S28]</sup>, that the formation of formic acid in the  
 146 laboratory was partly or entirely due to the decomposition of HMHP to HCOOH  
 147 + H<sub>2</sub>O. The precise extent to which this formation occurred by heterogeneous  
 148 reactions on the reactor walls is uncertain. A theoretical investigation<sup>[S30]</sup> con-  
 149 firmed that the reaction of H<sub>2</sub>COO with H<sub>2</sub>O leads to the formation of HMHP.  
 150 The predominant pathway in atmospheric conditions was found to be the reac-  
 151 tion with the H<sub>2</sub>O dimer: the rate constants for the reaction of H<sub>2</sub>COO with  
 152 the H<sub>2</sub>O monomer and the water dimer were calculated to be 8.2 · 10<sup>-18</sup> and  
 153 1.46 · 10<sup>-12</sup> molec.<sup>-1</sup>cm<sup>3</sup>s<sup>-1</sup>, respectively.

154 Assuming that HMHP is the only product in the reaction of H<sub>2</sub>COO with  
 155 H<sub>2</sub>O, HMHP yields in the ozonolysis of C<sub>2</sub>H<sub>4</sub> (0.37), C<sub>3</sub>H<sub>6</sub> (0.16), MVK (0.32)  
 156 and MACR (0.22) are adopted, based on the [H<sub>2</sub>COO]\* stabilisation fraction

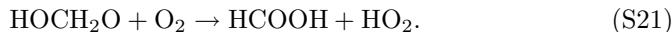
157 observed for  $\text{C}_2\text{H}_4 + \text{O}_3$  (0.37) and on the IUPAC recommendation<sup>[S25]</sup> for  
 158 the  $[\text{H}_2\text{COO}]^*$  branching ratio in the alkene + ozone reaction. For isoprene, we  
 159 adopt the average HMHP yield from two studies (0.23)<sup>[S24, S31]</sup>. The case of  
 160 monoterpenes is discussed in the subsection 2.3.

161 HMHP has been commonly observed at levels comparable to those of methyl  
 162 hydroperoxide in the boundary layer over isoprene-rich areas<sup>[S32, S33, S34, S35]</sup>,  
 163 supporting the view that isoprene and other biogenic alkenes are an impor-  
 164 tant source of HMHP. These observations also show that fast decomposition  
 165 of HMHP is unlikely at atmospheric conditions. We therefore neglect HMHP  
 166 decomposition in the model. Should some decomposition (to  $\text{HCOOH} + \text{H}_2\text{O}$ )  
 167 occur, our assumption would not lead to a large underestimation of  $\text{HCOOH}$   
 168 formation, because the atmospheric degradation of HMHP leads primarily to  
 169  $\text{HCOOH}$  anyway, as detailed below.

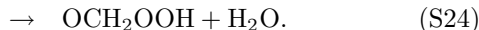
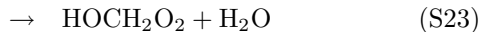
170 HMHP photolysis proceeds by cleavage of the peroxidic bond<sup>[S25]</sup>:



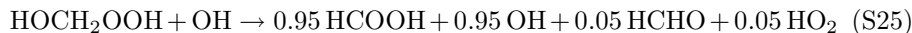
171 which is immediately followed by



172 The HMHP absorption cross sections are slightly lower than those of methyl  
 173 hydroperoxide<sup>[S36]</sup>, which makes photolysis a very minor sink. Reaction with  
 174 OH proceeds by H-abstraction from the carbon, from the hydroperoxide or from  
 175 the hydroxy group<sup>[S37]</sup>:



176 In lower tropospheric conditions,  $\text{HOCH}_2\text{O}_2$  decomposes thermally to  $\text{HCHO}$   
 177 and  $\text{HO}_2$ <sup>[S38, S39]</sup>. The radicals formed in Reactions (S22) and (S24) decom-  
 178 pose rapidly to  $\text{HCOOH} + \text{OH}$ <sup>[S40]</sup> and  $\text{HC(O)OOH} + \text{H}$ , respectively<sup>[S37]</sup>.  
 179 The first channel (Reaction S22) is by far dominant<sup>[S37]</sup>, as confirmed by the  
 180 experimental  $\text{HCOOH}$  yield<sup>[S36]</sup> of 95% in the reaction of HMHP with OH. As  
 181 the stronger hydroxy O–H bond should keep the third channel negligible, we  
 182 write Reactions (S22)-(S24) as



183 with an adopted reaction rate of  $3 \cdot 10^{-11} \text{ molec.}^{-1} \text{ cm}^3 \text{ s}^{-1}$ .

184 HMHP also undergoes dry and wet deposition. Dry deposition is calculated  
 185 using the deposition velocity calculated for  $\text{H}_2\text{O}_2$ . The parameterisation of  
 186 wet deposition accounts for the high Henry’s law’s constant of HMHP<sup>[S41]</sup>,  
 187  $1.24 \cdot 10^{-8} \exp(9700/T) \text{ M atm}^{-1}$ .



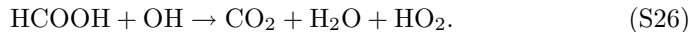
188 An additional loss process for HMHP is provided by its dissolution in liq-  
 189 uid cloud droplets followed by (water-assisted) decomposition to HCHO +  
 190 H<sub>2</sub>O<sub>2</sub>[S41, S42]. Whereas the decomposition lifetime is less than an hour at  
 191 neutral pH conditions, it is relatively slow at typical pH values found in clouds  
 192 (4-5), with a lifetime ranging between several hours and several days[S42]. It is  
 193 therefore neglected in the model.

## 194 2.3 Oxidation of monoterpenes

195 HMHP can also be produced in the ozonolysis of exo-cyclic (or epi-cyclic)  
 196 monoterpenes (e.g.  $\beta$ -pinene and sabinene[S25], but not  $\alpha$ -pinene). For such  
 197 large alkenes, decomposition of the primary ozonide to HCHO and a large  
 198 Criegee intermediate (reaction S19) is largely dominant (> 80%)[S43]. In this  
 199 case, even though the energy channelled to [H<sub>2</sub>COO]\* in the minor ozonolysis  
 200 route (reaction S18) is at most a few kcal/mol, such that all will be stabilized,  
 201 the yield of HMHP remains small, of the order of 20% or less. This formation is  
 202 neglected in the model. Instead, a direct HCOOH formation is assumed, with a  
 203 yield of 10% in the reactions of monoterpenes with O<sub>3</sub> and OH, to account for  
 204 the possible but very uncertain formation of HCOOH, mostly from secondary  
 205 chemistry, in the still largely unexplored chemical mechanism of monoterpenes.  
 206 First-generation molar yields of formic acid were found to range between 2  
 207 and 11% in laboratory studies of monoterpene oxidation by OH[S44, S45] and  
 208 O<sub>3</sub>[S46]. Evidence for higher yields due to the further degradation of the primary  
 209 products is provided by the OH-initiated monoterpene oxidation experiments  
 210 of Larsen *et al.*[S47]. Yields ranging between 28% (for  $\alpha$ -pinene) and 54% (for  
 211 limonene) were obtained after 20 minutes of intense photooxidation. Since the  
 212 total yield of identified small organic compounds (HCOOH, HCHO, CO, CO<sub>2</sub>  
 213 and acetone) represented between 28% and 46% of the reacted terpene on a car-  
 214 bon basis in these experiments, the further oxidation of the remaining products  
 215 (i.e. 54-72% of the carbon flux) might bring the overall molar yield of HCOOH  
 216 in these laboratory conditions to much larger values, possibly of the order of  
 217 100%. Caution is required, however, since an unrealistic radiation source (Hg  
 218 lamp peaking at 254 nm) was used in these experiments, which probably caused  
 219 a strong photolysis of aldehydic compounds. Still, these results clearly suggest  
 220 that HCOOH is a likely end-product in a large number of terpene degradation  
 221 pathways.

## 222 3 Sinks of Formic Acid

223 The only gas-phase sink of formic acid is reaction with OH, represented in the  
 224 model as



225 Its rate expression,  $k=2.27 \cdot 10^{-14} \cdot \exp(786/T) + 9.85 \cdot 10^{-13} \cdot \exp(-1036/T)$  im-  
 226 plies higher rate values in the cold upper troposphere, compared to boundary

227 layer conditions<sup>[S7]</sup>. The use of a temperature-independent rate<sup>[S25]</sup> will be  
 228 tested in a sensitivity inversion, as described in Section 8.

229 The dry deposition velocity over land is parameterised as a function of the  
 230 leaf area index (LAI) obtained from MODIS<sup>[S48]</sup>. It increases linearly from 0  
 231 to  $1.2 \text{ cm s}^{-1}$  for an LAI of  $6 \text{ m}^2 \text{ m}^{-2}$ . Wet scavenging is calculated based on  
 232 ECMWF precipitation, cloud fraction and convective updraft fields<sup>[S49]</sup>. The  
 233 effective Henry’s law constant (in  $\text{M atm}^{-1}$ ) is calculated with<sup>[S50, S51]</sup>

$$K_{H,\text{eff}} = [2.5 \cdot 10^{-5} \cdot \exp(5700/T)] \cdot (1 + 1.8 \cdot 10^{-3}/[\text{H}^+]) \quad (\text{S27})$$

234 and assuming a pH of 4.5.

235 Finally, the effect of reversible uptake by ice clouds is also considered. Par-  
 236 titioning to ice particles is calculated with

$$[X_s]/[X_g] = S_{\text{ice}} \cdot K_{\text{linC}} \quad (\text{S28})$$

237 with  $[X_s]$  and  $[X_g]$  the ice surface and gas phase concentrations, respectively (in  
 238  $\text{molec.cm}^{-3}$ ),  $S_{\text{ice}}$  the surface area density of ice ( $\text{cm}^2 \text{ cm}^{-3}$ ) and  $K_{\text{linC}}$  (in cm)  
 239 the partitioning coefficient in the linear regime of the adsorption isotherm<sup>[S52]</sup>

$$K_{\text{linC}} = 4 \cdot 10^{-12} \cdot \exp(7000/T), \quad (\text{S29})$$

240 where it has been taken into account that the fractional surface coverage ( $\theta =$   
 241  $K_{\text{linC}} \cdot [X_g]/N_{\text{max}}$ ) is much less than unity in atmospheric conditions. The ice  
 242 surface area density is parameterised based on the ice water content (IWC, in  
 243  $\text{g m}^{-3}$ ) assuming a scaling ratio of 10 between the cross-sectional area and the  
 244 surface area density<sup>[S53, S54]</sup>:

$$S_{\text{ice}} = 10^{-3} \cdot \text{IWC}^{0.9} \quad (\text{S30})$$

245 The effect of cirrus gravitational settling on the vertical distribution of HCOOH  
 246 is estimated using Eq. (S28) and the parameterisation of the ECMWF IFS model  
 247 for the ice settling velocity<sup>[S49]</sup>. This effect, however, is found to be very small.

## 248 4 Organic Aerosol Modeling in IMAGESv2

249 This section presents the organic aerosol module in the model. The heteroge-  
 250 neous oxidation of organic aerosols by OH is assumed to generate HCOOH in  
 251 the F2 run (Table 1). Three sources of organic aerosol (OA) are considered :

- 252 • Direct emission of Primary Organic Aerosol (POA) due to anthropogenic  
 253 sources<sup>[S55]</sup> ( $13.5 \text{ TgC/year}$  or  $23.6 \text{ Tg/year}$ ) and biomass burning<sup>[S9]</sup>  
 254 ( $12.2 \text{ TgC/year}$  or  $21.3 \text{ Tg/year}$ ). POA has hydrophilic and hydrophobic  
 255 components. Conversion of hydrophobic to hydrophilic POA due to aging  
 256 is represented by an e-folding time of 1 day<sup>[S56]</sup>.

- Reversible Secondary Organic Aerosol (SOA) formation due to the partitioning of semi-volatile organic compounds. We adopt the approach of the two-product model<sup>[S57, S58]</sup> for estimating this production of SOA from isoprene, terpenes and aromatics. The product yields and partitioning parameters of the condensable compounds from aromatics<sup>[S57]</sup>, isoprene<sup>[S59]</sup> and sesquiterpenes<sup>[S58]</sup> are based on laboratory data. For monoterpenes, we adopt a ten-product model<sup>[S60]</sup>, with parameters derived from simulations using a detailed  $\alpha$ -pinene oxidation and SOA formation model (BOREAM)<sup>[S61, S62]</sup>. The model accounts for a dependence of the yields on the NO<sub>x</sub> regime and on the nature of the primary oxidant (O<sub>3</sub>, OH or NO<sub>3</sub>). The partitioning coefficients (not only for  $\alpha$ -pinene SOA, also for other condensable compounds) are corrected to account for water uptake, based on BOREAM model simulations<sup>[S60]</sup>.
- Irreversible SOA formation due to the production of essentially non-volatile compounds (e.g. oligomers and polymers). In IMAGESv2, the formation of SOA from glyoxal and methylglyoxal is included as an irreversible process<sup>[S63, S49]</sup>. It is assumed to be very fast in liquid clouds. On aqueous aerosols, a constant reactive uptake coefficient ( $2.9 \cdot 10^{-3}$ ) is assumed.

The model accounts for wet and dry deposition of aerosols and aerosol precursors. The wet removal scheme<sup>[S49]</sup> is based on ECMWF cloud and precipitation data. The semi-volatile gaseous SOA precursors are assumed to be as water-soluble as glyoxal, given the high solubility of typical multi-functional SOA components.

The global SOA source calculated by IMAGESv2, ca. 100 Tg/year, compares well with the recent estimate of  $140 \pm 90$  Tg/year derived from aerosol mass spectrometer (AMS) measurements<sup>[S64]</sup>. Note however that our modelled SOA is overwhelmingly (> 90%) biogenic, whereas AMS measurements suggest a large (100 Tg/year) anthropogenically-controlled contribution. Comparisons with surface OC concentrations measurements of the IMPROVE (Interagency Monitoring of Protected Visual Environments)<sup>[S65]</sup> and EMEP (European Monitoring and Evaluation Programme)<sup>[S66]</sup> network suggests that our modelled SOA source is overestimated by almost a factor of two over the Eastern US during summertime and that it is largely underestimated over Europe.

## 5 Ground-based and Aircraft Measurements

To evaluate the model performance, we use Fourier Transform Infrared (FTIR) column measurements of HCOOH at Wollongong in southeast Australia (34.41 S, 150.88 E), and Reunion Island in the southern Indian Ocean (21 S, 55 E)<sup>[S7]</sup>. The retrievals adopted the improved spectroscopic parameters for the HCOOH  $\nu_6$  absorption band near  $1105.4 \text{ cm}^{-1}$  (HITRAN 2008)<sup>[S67, S68]</sup>.

Further, we use a compilation of in situ concentration measurements in surface air and in precipitation water (Tables S2, S3 and S4). The observed concentrations are compared with the modelled concentrations in 2009, interpolated at the measurement locations and averaged over the same months (Figs. S6, S7). The significant dispersion before and after optimisation most likely reflects the large spatiotemporal variability of HCOOH and the limited representativity of local measurements from many different years in comparison with model values for 2009 at  $4^\circ \times 5^\circ$  resolution. When considering all measurements, the correlation coefficient is equal to 0.5 for surface air concentrations and 0.3 for precipitation water concentrations in the a priori simulations. After optimisation, the correlation coefficient for both air and water concentrations is equal to ca. 0.45.

Aircraft campaign measurements of HCOOH from three expeditions are also used for comparisons (Fig. S8) :

1. The PEM-Tropics A (Pacific Exploratory Mission-Tropics A) mission conducted in August-October 1996 as part of NASA's Global Tropospheric Experiment (GTE) with focus on the remote tropical regions of the Pacific ocean. The data, compiled onto a  $5 \times 5$  degrees grid with a vertical resolution of 1 km<sup>[S69]</sup>, can be accessed through the data composites web page ([http://acd.ucar.edu/~emmons/DATACOMP/camp\\_table.htm](http://acd.ucar.edu/~emmons/DATACOMP/camp_table.htm)).
2. The SONEX (Subsonic assessment, Ozone and Nitrogen oxide EXperiment) airborne field campaign conducted between October and November 1997 aboard a DC-8 NASA aircraft in the vicinity of the North Atlantic flight corridor<sup>[S70]</sup>.
3. The National Aeronautical Space Administration (NASA) Intercontinental Chemical Transport Experiment, Phase B (INTEX-B) aircraft mission conducted in spring 2006 (1 March to 15 May) over the region of Mexico in March (first phase) and over the Pacific in April and May (second phase)<sup>[S71]</sup>.

A comparison between the observed and the modelled HCOOH concentrations averaged over large regions before and after optimisation is provided in Table S5.

## 6 Uncertainties on IASI HCOOH columns

The error of 60% on the IASI HCOOH columns is a theoretical error based only on forward simulations for an individual measurement. Other sources of error include propagating errors from level 2 data (e.g. total water column, thermal contrast) and possible bias errors, such as uncertainty in the assumed profile of formic acid or on the spectroscopy. The total error can only be rigorously quantified with an extensive validation of the IASI columns but unfortunately

335 there are currently few correlative measurements of the formic acid total columns  
336 for such an analysis.

337 An explicit comparison with FTIR ground-based measurements at Wollon-  
338 gong and Reunion Island site (Figure 2 of the letter and Fig. S11) shows a high  
339 degree of correlation ( $R^2 = 0.84$ ). Data from other FTIR sites, like Thule and  
340 Bremen have been obtained from Figs. 3 and 4 of Ref. [S7]. However, at these  
341 sites spatially co-located IASI measurements are not available for comparison,  
342 unless a very large  $8^\circ \times 8^\circ$  area is considered around each station, making the  
343 comparison of very little value for validation. From these restricted comparisons  
344 there is thus no indication for a significant IASI overall bias.

345 The error adopted in the inversions consists in an absolute error of  $4 \times 10^{15}$   
346 molec.cm $^{-2}$  and a 30% relative error. This was chosen in order to avoid overly  
347 optimistic error bars for the low concentrations. We acknowledge the crudeness  
348 of this error estimate, and therefore, sensitivity inversions using either doubled  
349 or halved errors were performed. These tests are presented and discussed in  
350 Section 8.

## 351 7 Impact on Precipitation Acidity

352 The pH of precipitation is estimated in the model based on the wet deposition  
353 fluxes of  $\text{HNO}_3/\text{NO}_3^-$ ,  $\text{SO}_4^{2-}$ ,  $\text{NH}_3/\text{NH}_4^+$ ,  $\text{CO}_2/\text{HCO}_3^-$  and the carboxylic  
354 acids  $\text{HCOOH}$  and  $\text{CH}_3\text{COOH}$ , accounting for their respective dissociation con-  
355 stants,  $1.8 \cdot 10^{-4}$  and  $1.8 \cdot 10^{-5}$  mol/L [S51]. Dust aerosols, and therefore, alkaline  
356 components such as  $\text{Ca}^{2+}$ ,  $\text{Na}^+$  and  $\text{K}^+$ , are neglected in the model, leading to  
357 a likely underestimation of precipitation pH.

## 358 8 Sensitivity Inversions

359 This section explores the impact of possible errors in key model parameters on  
360 the inversion results. In each sensitivity inversion (Table S6), a parameter or  
361 input dataset of the Opt2 standard optimisation is varied, and new emissions are  
362 obtained. The resulting global emissions and sinks are summarised in Table S7.

363 Acknowledging the broad IASI column error estimate used in the reference  
364 optimisations (see “Methods” section), additional inversions were performed  
365 using either doubled (Opt2-Errx2) or halved (Opt2-Err:2) IASI errors. Chang-  
366 ing these errors affects the balance between the first term of the cost function  
367 (cf. Eq. (1), “Methods” section) representing the model-data bias and the  
368 second term which measures how far the optimised emissions are from the a  
369 priori. Halving the errors results in an almost negligible increase (6% globally).  
370 Doubling the IASI column errors leads to a decrease (13%) in the optimised  
371 emissions, as the optimisation is more constrained by the a priori. The latitu-  
372 dinal distribution of the emissions (Fig. S12) remains unaffected, except in the  
373 summertime Southern hemisphere in the  $20^\circ$ - $35^\circ$  S band, where the optimisa-  
374 tion results appear less robust. However, the comparison with ground-based

375 FTIR data at Wollongong (Fig. 2) indicates that IASI errors are not likely to  
376 be larger than our reference estimates.

377 Dry deposition accounts for about one third of the global HCOOH sink in  
378 IMAGESv2, based on a simple parameterisation. The contribution of dry de-  
379 position could be higher, however, as reactive uptake by vegetation has been  
380 recently shown to enhance the deposition of many oxygenated VOCs<sup>[S72]</sup>. We  
381 therefore conducted a source inversion with HCOOH deposition velocities over  
382 land increased by 50% (Opt2-Dry). In spite of this strong increase, the inferred  
383 global HCOOH emission is increased by only 6% (Table S7), because dry de-  
384 position over land represents only a relatively small fraction of the global sink,  
385 and because the stronger surface sink reduces the vertical tropospheric gradient  
386 and therefore the surface HCOOH concentrations.

387 Uncertainties related to wet scavenging (about 38% of the global HCOOH  
388 sink in IMAGESv2) include uncertainties in the meteorological fields and in the  
389 gas/liquid partitioning ratio for HCOOH, calculated from the effective Henry’s  
390 law constant for HCOOH, itself dependent on pH. Using an alternative dataset  
391 for convective and stratiform precipitation (the NCAR/NCEP Reanalysis<sup>[S73]</sup>)  
392 (<http://www.esrl.noaa.gov/psd/>) in inversion Opt2-NCEP results in a longer  
393 HCOOH lifetime with respect to wet deposition (10.5 vs. 12.2 days), primarily  
394 because stratiform precipitation in NCEP is much less widespread at tropical  
395 latitudes, compared to ERA-Interim fields. This change has however only very  
396 little impact on the optimised HCOOH emissions, cf. Table S7.

397 Including an on-line dynamical calculation of cloud pH in the model leads to  
398 a negligibly (3%) longer HCOOH lifetime, compared to the reference model cal-  
399 culations assuming pH=4.5. However, the pH might be underestimated, given  
400 that alkaline components from e.g. dust are neglected. The results of opti-  
401 misation Opt2-pH5, assuming pH=5, indicate a low sensitivity of the overall  
402 HCOOH sink to the cloud pH: the global lifetime is decreased by about 5%,  
403 and the global HCOOH source needed to match the IASI column measurements  
404 is increased by about 4 Tg yr<sup>-1</sup>.

405 The rate used in the model for HCOOH+OH, and obtained from a theoret-  
406 ical study<sup>[S74]</sup>, implies a negative temperature dependence in the atmospheric  
407 range, leading to higher rates in the upper troposphere. However, laboratory  
408 measurements conducted at and above 297 K (IUPAC recommendation<sup>[S25]</sup>)  
409 indicate a negligible temperature dependence. The sensitivity inversion Opt2-  
410 kOH conducted with the IUPAC recommendation ( $4.5 \cdot 10^{-13}$  molec.<sup>-1</sup>cm<sup>3</sup> s<sup>-1</sup>,  
411 independent of temperature) leads to a 7% increase of the global HCOOH life-  
412 time, in spite of the higher value of the rate in the lower troposphere. The  
413 global biogenic source of HCOOH is decreased by almost 4 Tg yr<sup>-1</sup> (i.e. by 4%)  
414 compared to the reference optimisation.

415 The isoprene chemical mechanism used in the model includes peroxy radical  
416 isomerisations leading to compounds (hydroperoxy-enones) for which the sub-  
417 sequent chemistry remains largely unexplored; furthermore, the isomerisation  
418 rates are themselves uncertain. In optimisation Opt2-Isom, these isomerisa-  
419 tions are simply ignored. This mechanistic change increases the production

420 of HCOOH due to isoprene oxidation by  $5.7 \text{ Tg yr}^{-1}$ , mostly due to enhanced  
 421 HCOOH formation through (1) the epoxide channel of the isoprene peroxy, and  
 422 (2) HMHP formation due to isoprene ozonolysis. The contribution of ozonolysis  
 423 to the isoprene sink is increased from 8% to 14.5% when the 1,6 H-shifts are  
 424 suppressed, due to lower OH abundances over forested areas. The global pro-  
 425 duction of isoprene epoxides is increased from 40 to 106 Tg annually. Isoprene  
 426 ozonolysis and the epoxide oxidation by OH are both significant pathways to  
 427 HCOOH formation in our mechanism. An additional effect of the mechanistic  
 428 change is the increased overall lifetime of HCOOH, from 4.3 to 4.6 days, also  
 429 due to the lower OH levels calculated when the isomerisation reactions of the  
 430 isoprene peroxy are ignored. Note that the higher OH levels calculated with the  
 431 LIM0 mechanism are supported by comparisons with observations over Ama-  
 432 zonia and over the US<sup>[S4]</sup>. As a consequence of the higher formation rate and  
 433 overall lifetime of HCOOH in this sensitivity inversion, the annual global source  
 434 needed to match the IASI measurements is slightly decreased from 102 to 98  
 435 Tg.

436 The optimisation results for the biogenic HCOOH source are also dependent  
 437 on assumptions for the pyrogenic source, also retrieved in the optimisations.  
 438 E.g. increasing the pyrogenic a priori emissions, or increasing the fraction of  
 439 biomass burning emissions released at high altitudes, where HCOOH is longer-  
 440 lived, could in principle increase the contribution of fires to the total column,  
 441 thereby reducing the need for large biogenic emissions. The optimisation Opt2-  
 442 Inj uses a fire injection profile<sup>[S75]</sup> with substantially higher fractions injected  
 443 in the middle (30%) and upper (30%) troposphere, compared to the profile<sup>[S76]</sup>  
 444 used in IMAGESv2. The results (Table S7) show that the vertical distribution  
 445 of pyrogenic emissions has only a negligible influence on the derived budget and  
 446 lifetime. The optimised global emissions due to vegetation fires is decreased  
 447 (from 4.0 to  $3.5 \text{ Tg yr}^{-1}$ ) when adopting the alternative injection height profile,  
 448 as a consequence of the longer lifetime of formic acid at higher altitudes. This  
 449 confirms the minor role played by vegetation fires in determining the HCOOH  
 450 column distribution.

451 In conclusion, the optimisation results appear to be robust, since the an-  
 452 nual global biogenic source is found to range between 77 and 96 Tg, when the  
 453 additional HCOOH production is assumed to be secondary. The lowest emis-  
 454 sions ( $77 \text{ Tg yr}^{-1}$ ) are obtained when assuming unrealistically large errors on  
 455 the IASI column data. Still, it must be acknowledged that the real uncertainty  
 456 might be larger, since the above sensitivity experiments cannot possibly cover  
 457 the full range of possible uncertainties.

## 9 Tables

Table S1: Mean percentage biases (model-observations) and correlation coefficients calculated for the standard model simulation F1 and the Opt2 inversion constrained by IASI data. Results from the Opt1 inversion are very similar to those from Opt2 and are not shown here.  $N$  is the number of observational elements used in the inversion, i.e. monthly averaged IASI HCOOH columns at the resolution of the model.

<i>Region</i>	<i>N</i>	<i>Mean bias</i>		<i>Correlation coefficient</i>	
		F1	Opt2	F1	Opt2
N.America 30-70 N, 60-170 W	475	-80.8	-11.0	0.43	0.72
Tropical America 30 S-20 N, 30-80 W	489	-72.3	-12.5	0.84	0.91
Africa 40 S-30 N, 20 W-45 E	814	-71.7	-10.8	0.75	0.93
Asia 10 S-55 N, 60-160 E	856	-73.2	-14.2	0.34	0.80
Oceania 40 S-10 N, 110-170 E	402	-72.9	-14.1	0.44	0.84
Boreal (55-88 N)	419	-85.8	-13.4	0.33	0.71
Tropics (25 S-25 N)	1869	-70.5	-12.2	0.70	0.91
Globe	3768	-75.4	-13.6	0.59	0.87



Table S2: In situ measurements of HCOOH mixing ratio expressed in pptv.

<i>Location</i>	<i>Coordinates</i>	<i>Period</i>	<i>HCOOH</i>	<i>Ref.</i>
<i>North America</i>				
Mt. Lemmon, Tucson	32.4N 249.2E	Feb	130	[S77]
Socorro, New Mexico	36N 254E	Jun-Aug	700	[S78]
Langmuir, New Mexico	33.9N 253E	Jun-Aug	600	id.
id.	id.	Jun-Aug	1050	id.
Pagosa Springs, Colorado	37.2N 253E	Jun	1310	[S77]
Wolf Creek, Colorado	37.5N 253.3E	Jun	1190	id.
NW Dakota	45.5-49N			
	256-260E	Jun	2640	id.
id.	id.	Jul	1810	id.
id.	id.	May	110	id.
Oregon, Cape Meares	45.5N 236E	Sep	180	id.
id.	id.	Oct	60	id.
Pensylvania	41N 283E	Jul-Aug	2500	[S79]
Charlottesville, Virginia	38N 281.7E	Jun	1820	[S80]
Shenandoah park, Virginia	38N 281.7E	Sep	5400	[S81]
Virginia	37N 283.7E	Mar-Sep	1890	[S82]
Virginia	id.	Oct-Feb	695	id.
<i>South America</i>				
Venezuelan savannah	8N 297E	Apr	450	[S83]
Venezuelan savannah	8.5N 298E	Sep	450	[S84]
N. Venezuela	10.5N 293E	Mar	1700	[S85]
id.	id.	Jun	710	id.
id.	id.	Oct	960	id.
id.	id.	Dec	610	id.
La Selva, Costa Rica	10.4N 276.1E	Apr-May	905	[S86]
Central Amazonia	4S 300E	Jul-Aug	1590	[S87]
Rondonia, Brazil	10S 298E	May	1600	[S88]
id.	id.	Sep-Nov	10500	id.
Ducke Reserve-Manaus	3S 300E	Jul-Aug	1880	[S80]
id.	id.	Apr-May	510	[S89]
<i>Other regions</i>				
Schoeneben, Austria	48.7N 13.9E	Mar-Apr	1066	[S90]
id.	id.	Sep	620	id.
N.Congo rainforest	2N 18E	Feb	500	[S91]
Mayombe, SW Congo	4.5N 12.5E	Jul-Aug	260	[S92]
Dayalbagh, India	28.5N 77.2E	Jan-Dec	1700	[S93]
id.	id.	May-Oct	1300	id.
id.	id.	Nov-Apr	1800	id.
Gopalpura, India	27N 78E	Jul-Sep	1700	[S94]

Table S3: In situ measurements of HCOOH concentration in precipitation ( $\mu\text{mol/L}$ , volume-weighted averages) in North and South America.

<i>Location</i>	<i>Coordinates</i>	<i>Period</i>	<i>HCOOH</i>	<i>Ref.</i>
<i>North America</i>				
Virginia	38.1N 281.2E	Apr-Sep	13.6	[S95]
Hampton, Virginia	38N 281.7E	Mar-Sep	6.8	[S82]
id.	id.	Oct-Feb	1.6	id.
Tennessee	35.5N 276.7E	Jan-Feb	1.0	[S96]
Tallahassee	30.5N 275.8E	Jun-Aug	18.2	[S80]
North Carolina	34.2N 282.1E	Jan-Dec	9.9	[S97]
North Carolina, 1987-89	id.	Apr-Sep	8.2	id.
North Carolina, 1987-89	id.	Oct-Mar	3.5	id.
North Carolina, 1996-98	id.	Apr-Sep	17.6	id.
North Carolina, 1996-98	id.	Oct-Mar	3.0	id.
Los Angeles, California	34.1N 241.6E	Jan-Dec	12.4	[S98]
<i>South America</i>				
Calabozo, Venezuela	8.9N 298.4E	Jan-Dec	6.5	[S99]
Parupa, Venezuela	5.7N 298.4E	Jan-Dec	6.3	[S100]
Luepa, Venezuela	5.9N 298.6E	Jan-Dec	4.2	id.
Kavanayen, Venezuela	5.6N 298.2E	Jan-Dec	2.1	id.
Yuruani, Venezuela	5N 298.8E	Jan-Dec	2.4	id.
Auyantepuy, Venezuela	5.9N 298E	Apr	4.2	[S101]
Canaima, Venezuela	6.3N 297.1	Apr	2.9	id.
J.del Tigre, Venezuela	8.7N 296.7E	Jan-Dec	8.2	[S84]
Central Amazonia	2.6S 300E	Jul-Aug	17.9	[S87]
Central Amazonia	2.6-3.1S 300E	Apr-May	3.2	[S102]
Balbina, Centr. Amazonia	1.9S 300.5E	Jan-Dec	0.5	[S103]
French Guyana	5N 306.9E	Jan-Dec	5.5	[S104]
Lake Calado, Brazil	3.2S 299.5E	Jan-Dec	2.9	[S105]
Acegua, Uruguay	32.1S 306E	Jan-Dec	7.6	[S106]
Melo, Uruguay	32.4S 306E	Jan-Dec	7.1	id.
Treinta y Tres, Uruguay	32.4S 306E	Jan-Dec	2.2	id.
Torres del Paine, Chile	51.1S 288E	Jan-Dec	5.5	[S107]

Table S4: As Table S3, for Africa, Europe and Asia-Australia.

<i>Location</i>	<i>Coordinates</i>	<i>Period</i>	HCOOH	<i>Ref.</i>
<i>Africa</i>				
Banizoumbou, Niger	13.5N 2.7E	Jun-Oct	4.7	[S108]
Amersfort, S. Africa	27.1S 30E	Jan-Dec	7.5	[S109]
L. Trichardt, S. Africa	23S 30E	Jan-Dec	12.9	id.
Lamto, Ivory Coast	6N 355E	Jan-Dec	11.1	[S104]
Zoetele, Cameroon	3.2N 12E	Jan-Dec	8.7	[S110]
Mayombe, Congo	4.5S 12.5E	Jun-Sep	10.0	[S92]
id.	id.	Jun-Oct	10.6	[S111]
id.	id.	Nov-May	6.3	id.
<i>Europe</i>				
Basque Coun., Spain	43N 357.4E	Mar-Sep	8.1	[S112]
id.	id.	Oct-Feb	3.8	id.
Faroe Isl., Denmark	62.1N 353E	summer	2.0	[S113]
Anholt Isl., Denmark	56.7N 11.5E	summer	15.0	id.
Galicja, Spain	42.5-43.2N			
	351.5-352.5E	Mar-Sep	12.7	[S114]
id.	id.	Oct-Feb	2.8	id.
Patras, Greece	38.2N 21.7E	Jan-Dec	3.8	[S115]
<i>Asia-Australia</i>				
Amsterdam Isl., Indian Oc.	37.8S 77.5E	Jan-Dec	3.2	[S116]
Dorrigo, SE Australia	30.3S 152.7E	Jan-Apr	4.6	[S117]
Bar.Tops, SE Australia	31.9S 151.6E	Jan-Apr	6.8	id.
Katherine, Australia	14.5S 132.3E	Sep-Apr	10.5	[S118]
Darwin Airport, Australia	12.5S 130.8E	Nov-Apr	4.9	[S119]
West Guizhou, China	26.3N 105.9E	Jun-Oct	4.6	[S120]
Lijiang, China	26.9N 100.2E	Jan-Dec	3.1	[S121]
Gopalpura, India	27N 78E	Jul-Sep	5.4	[S94]
Rampur, India, monsoon	27.2N 78.1E	Jul-Sep	5.1	[S122]

Table S5: Average HCOOH concentrations over large regions measured (a) at surface sites (Table S2) ; (b) in precipitation water (Table S3 and S4) ; (c) during aircraft campaigns (SONEX, INTEX-B and PEM-Tropics-A (PEM-TA), and (d) average HCOOH columns measured by FTIR. The data are compared with model results in simulations F1-F3 and in inversion experiments assuming either a biogenic source of primary (Opt1) or secondary (Opt2) origin (see Table 1).

	Obs.	F1	F2	F3	Opt1	Opt2
<i>(a) Mixing ratio in surface air (pptv)</i>						
North America	1150	220	340	400	840	680
South America	1820	290	350	820	1410	740
Other regions	1120	510	770	740	1790	1170
<i>(b) Concentration in precipitation water (<math>\mu\text{mol/L}</math>)</i>						
North America	8.7	1.3	1.9	2.3	4.7	4.5
Europe	6.9	0.7	1.2	0.9	3.2	3.0
South America	5.2	1.0	1.4	2.8	3.6	2.9
Africa	9.0	2.8	4.8	5.4	10.1	8.4
Asia-Australia	5.4	1.4	2.3	3.5	3.1	3.0
<i>(c) Aircraft campaign mixing ratio (pptv)</i>						
North America (SONEX)	94	31	49	39	110	130
Western US (INTEX-B)	490	66	100	88	360	230
Mexico (INTEX-B)	1550	180	300	320	580	440
North Pacific (INTEX-B)	140	28	58	32	94	120
N. Trop. Pacific (PEM-TA)	40	11	31	18	20	25
S. Trop. Pacific (PEM-TA)	89	19	44	36	46	57
<i>(d) Vertical columns (<math>10^{14} \text{ molec.cm}^{-2}</math>)</i>						
Reunion Isl., Indian Ocean	20	7.8	18	14	20	24
Wollongong, Australia	59	12.5	20	36	47.5	45

Table S6: Description of the performed sensitivity inversions.

<i>Description</i>	<i>Abbreviation</i>
Standard inversion with secondary HCOOH source	Opt2
Errors on IASI HCOOH columns doubled	Opt2-Errx2
Errors on IASI HCOOH columns halved	Opt2-Err:2
HCOOH deposition velocity increased by 50%	Opt2-Dry
Use precipitation fields from NCEP	Opt2-NCEP
Cloud water pH assumed equal to 5	Opt2-pH5
Use IUPAC recommendation for HCOOH+OH reaction rate	Opt2-kOH
Use alternative fire injection heights <sup>[S75]</sup>	Opt2-Inj
Suppress isomerisation of peroxy radicals from isoprene	Opt2-Isom

Table S7: Annual estimates of sources, sinks and global lifetime of HCOOH inferred by sensitivity inversions. Units are in Tg per year. The biogenic emission estimates represent the sum of the primary biogenic source and of the IASI-derived secondary biogenic source of HCOOH.

<i>Abbreviation</i>	Global emission	Biogenic emission	Dry dep.	Wet dep.	OH oxidation	Lifetime (days)
Opt2	102.4	90.0	33.6	40.0	28.4	4.30
Opt2-Errx2	89.3	76.7	29.2	35.5	24.6	4.26
Opt2-Err:2	108.0	95.0	35.5	42.5	30.0	4.28
Opt2-Dry	108.4	96.3	40.0	40.0	28.4	4.05
Opt2-NCEP	101.5	89.0	33.8	37.4	30.3	4.55
Opt2-pH5	106.4	94.2	33.1	45.2	28.1	4.08
Opt2-kOH	98.8	86.4	31.8	39.3	27.7	4.62
Opt2-Inj	102.2	90.3	32.5	39.7	29.5	4.32
Opt2-Isom	97.8	84.8	31.1	39.8	26.9	4.57

459 **10 Figures**

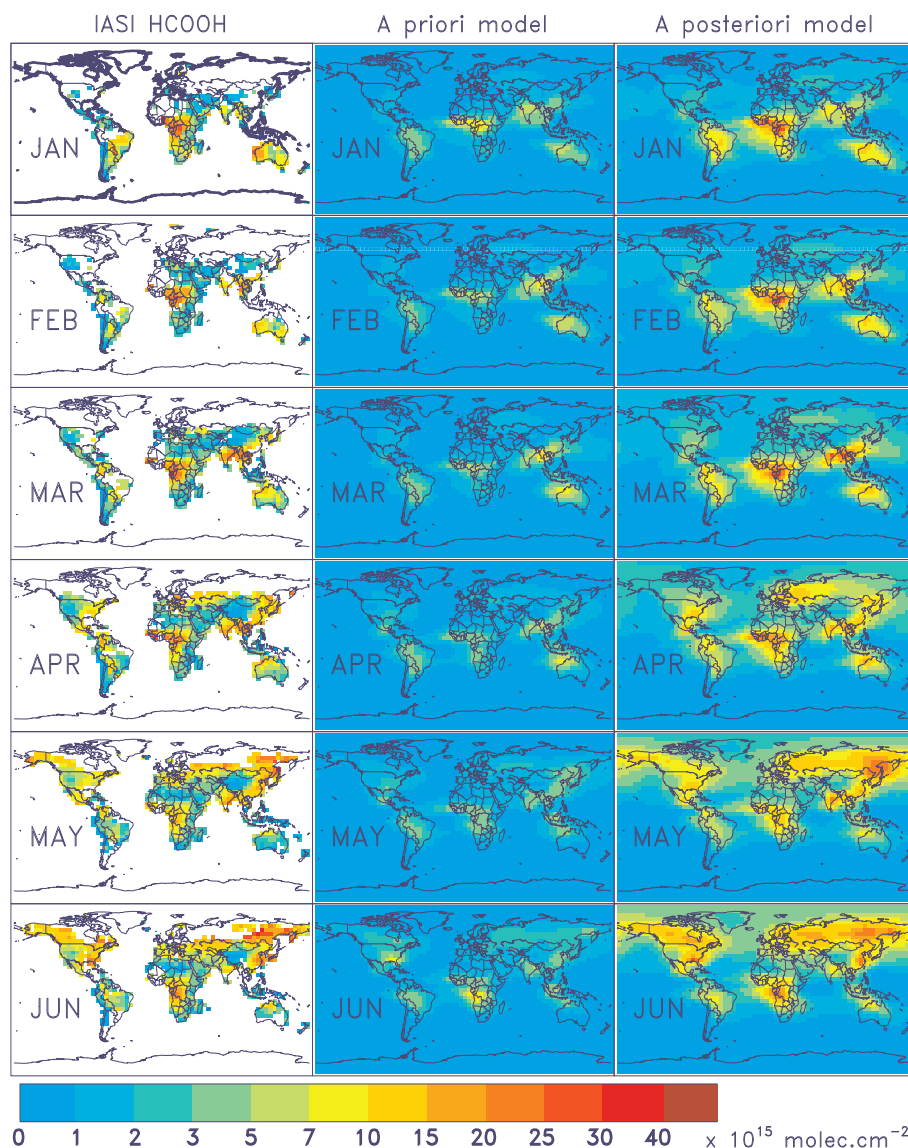


Figure S1: **Monthly averaged observed and modelled HCOOH columns between January and June 2009.** IASI columns (left column) are compared with a priori model columns (F1, middle) and optimised Opt2 HCOOH columns (right) inferred when a secondary HCOOH source of biogenic origin is assumed. Units are  $10^{15} \text{ molec.cm}^{-2}$ . Results from the Opt1 inversion are very similar to those from Opt2 and are not shown.

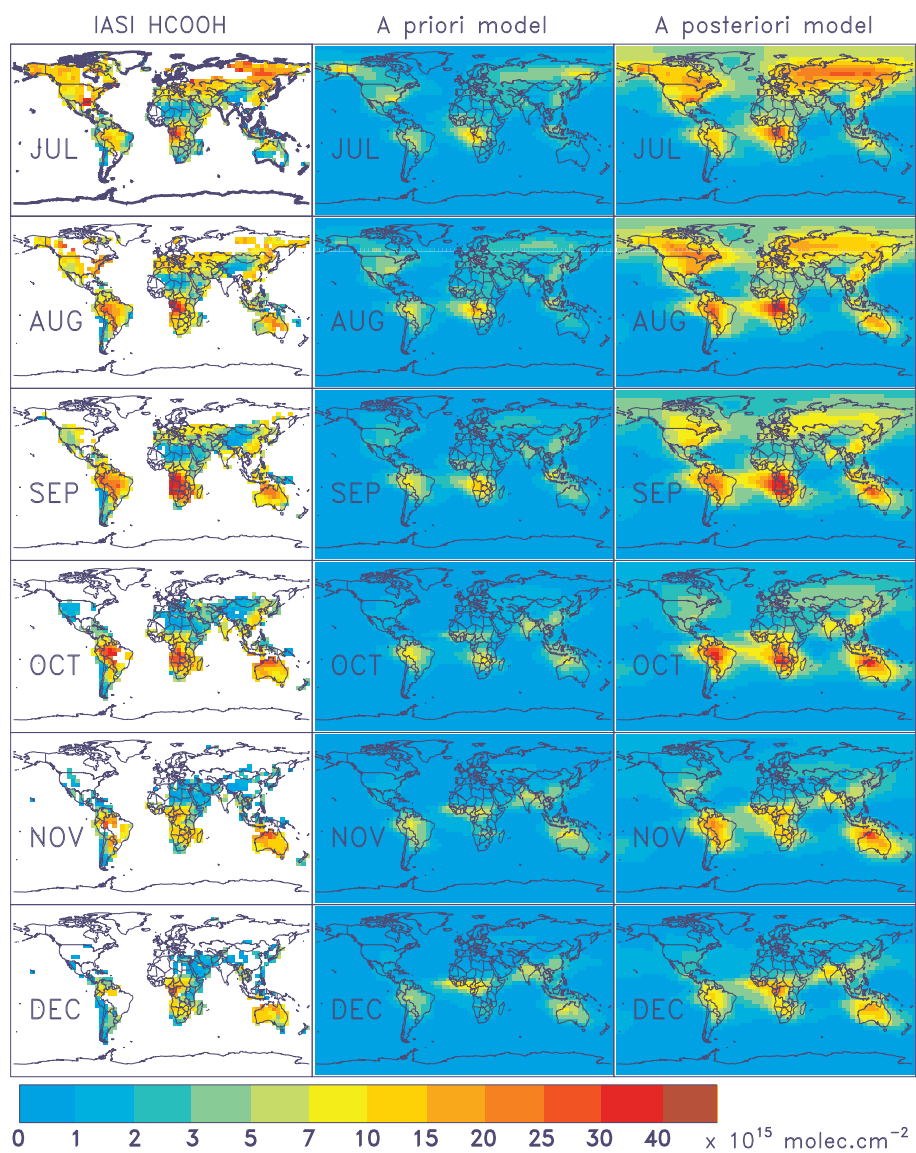


Figure S2: Same as Fig. S1, for July–December 2009.



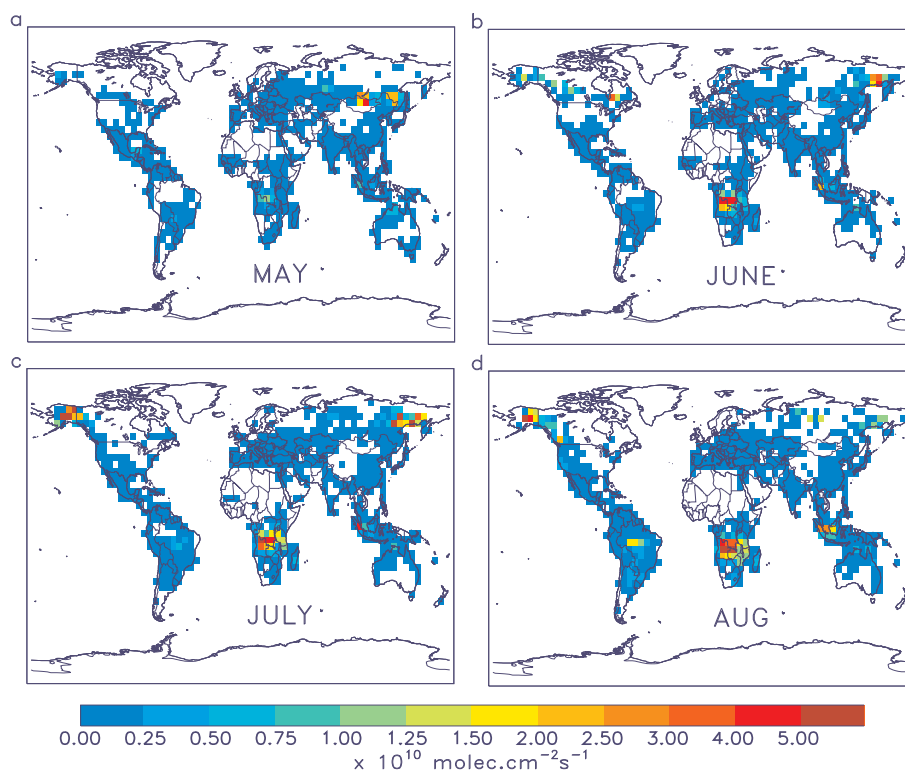


Figure S3: Monthly averaged emissions of HCOOH by biomass burning ( $10^{10}$  molec.cm<sup>-2</sup> s<sup>-1</sup>) from the GFEDv3 inventory<sup>[S9]</sup>. a, May. b, June. c, July. d, August. The fire locations on this figure generally do not coincide with enhanced HCOOH columns observed by IASI (see Fig. S1-S2), except to some extent in June in boreal regions.

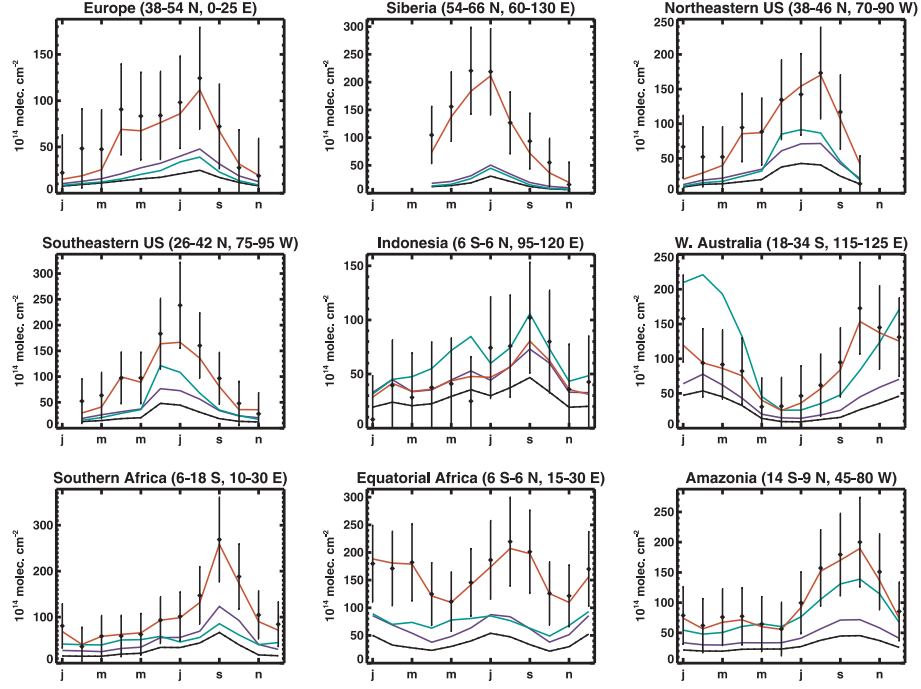


Figure S4: **Seasonal evolution over selected regions of monthly mean observed and modelled HCOOH columns.** IASI HCOOH columns (black diamonds) are compared with modelled columns of the F1 (black), F2 (purple), F3 (green), and Opt2 (red) simulations of Table 1. The error bars represent the assumed errors on IASI columns adopted in the source inversions. Results from Opt1 simulation are very close to Opt2 and are therefore not shown.

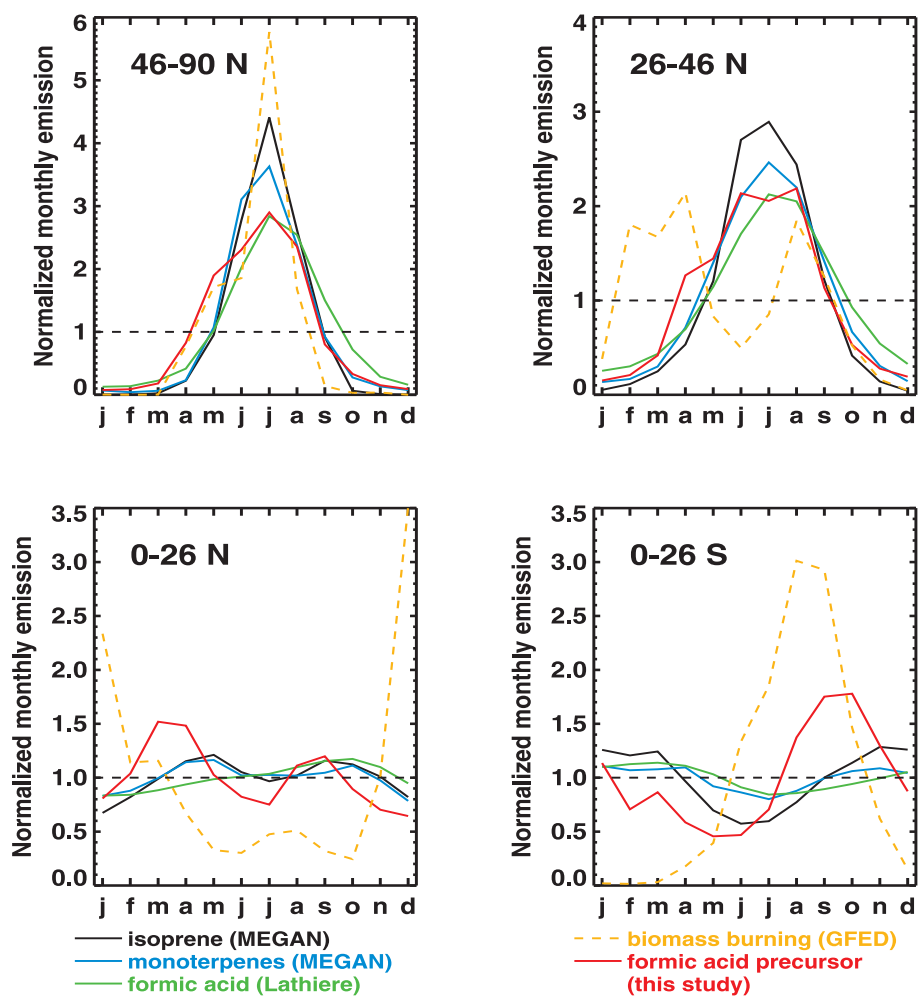


Figure S5: Monthly emissions (normalised by their annual average) for four latitude bands. Curves correspond to isoprene (in black), monoterpenes (blue), primary biogenic HCOOH (green), biomass burning HCOOH (orange), and the biogenic HCOOH precursor optimised in inversion Opt2 (red).

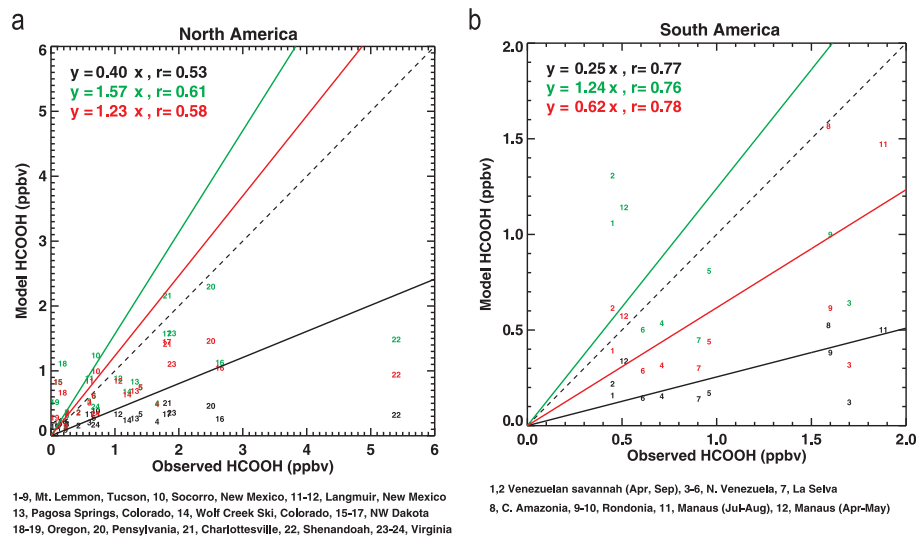


Figure S6: **Ground-based HCOOH mixing ratios at North and South American sites (Table S1) against model values.** Model concentrations are obtained at the same locations using the standard model (in black), and after optimisation assuming either a primary (in green) or a secondary (in red) biogenic source of HCOOH. The slopes of the regression lines indicated in the upper left corner are calculated as the arithmetic mean ratios of modelled to observed values. The correlation coefficient  $r$  for each region is given inset.

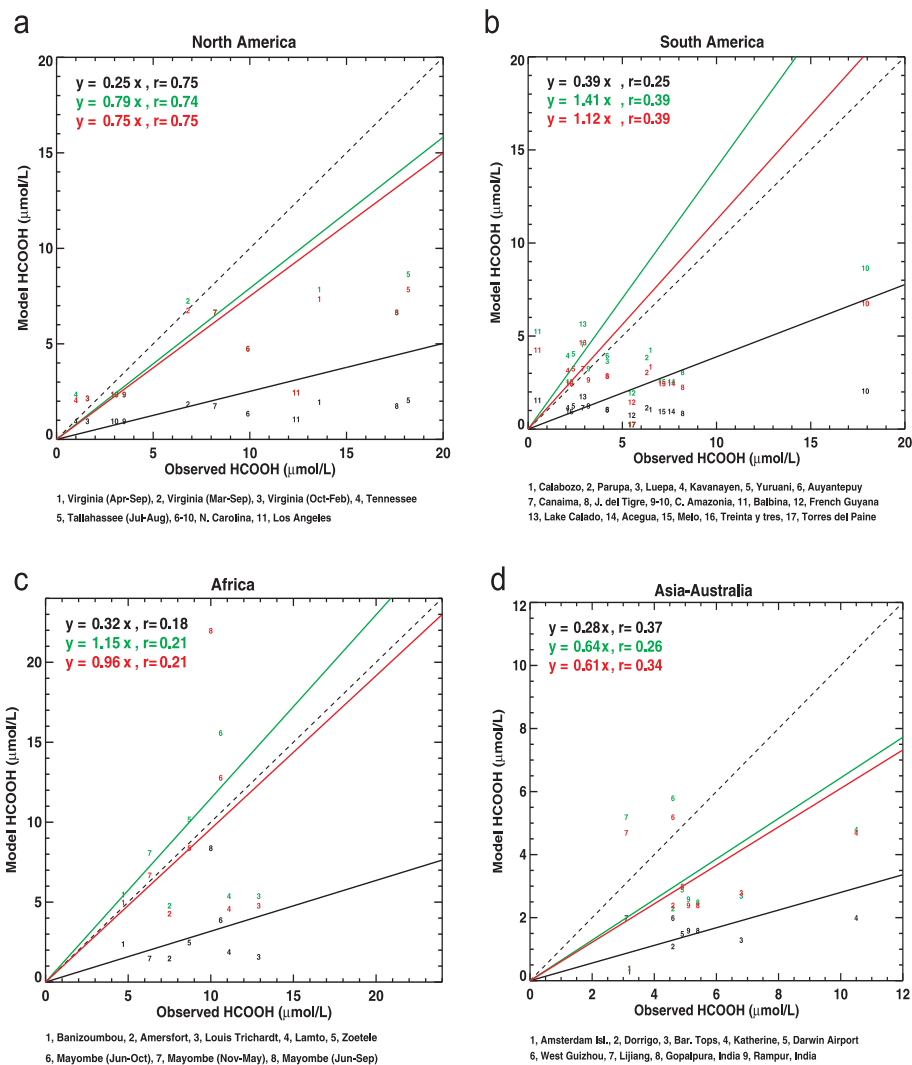


Figure S7: **Observed HCOOH concentrations in precipitation water against model values (Table S2 and S3) in different continents.** Color code is as in Fig. S6. The slopes of the regression lines indicated in the upper left corner are calculated as the arithmetic mean ratios of modelled to observed values. The correlation coefficient  $r$  for each region is given inset.

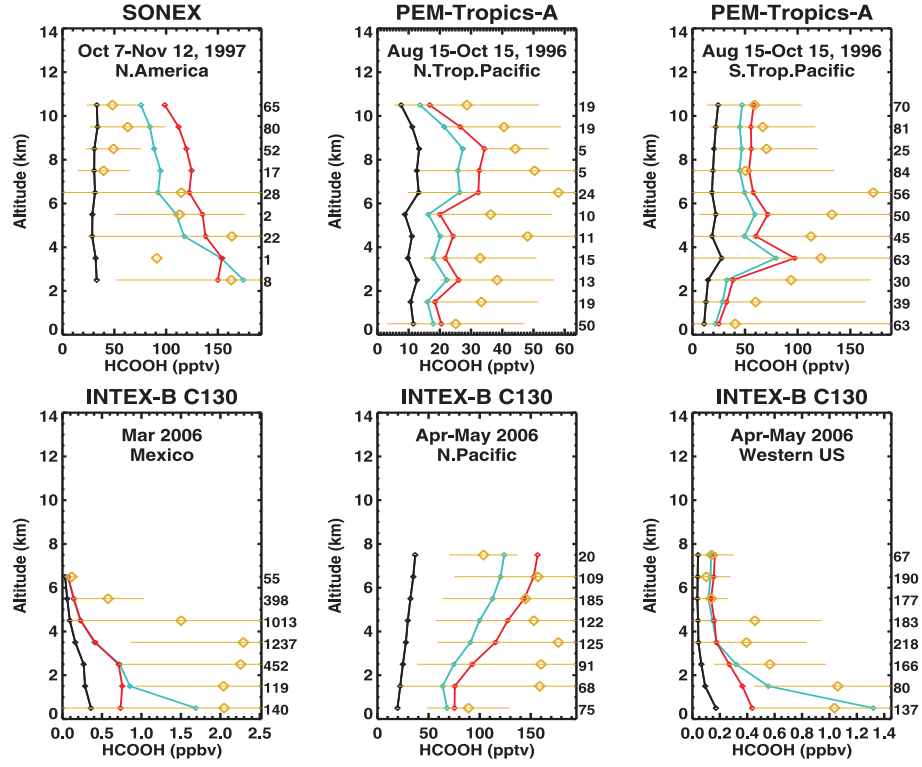


Figure S8: **Observed and modelled vertical distributions of HCOOH concentrations.** SONEX, PEM-Tropics-A and INTEX-B aircraft data over North America (25-55 N, 45-130 W), Mexico (0-25 N, 85-110 W), Western US (35-45 N, 105-125 W), North Pacific (25-55 N, 160-230 E), North Tropical Pacific (0-25 N, 180-275 W), and South Tropical Pacific (0-25 S, 180-275 W) are compared with model output in 2009 from the standard simulation F1 (black) and from Opt1 (green) and Opt2 (red). The number of observations at each altitude bin is given on the right end of each plot. Error bars are standard deviations.

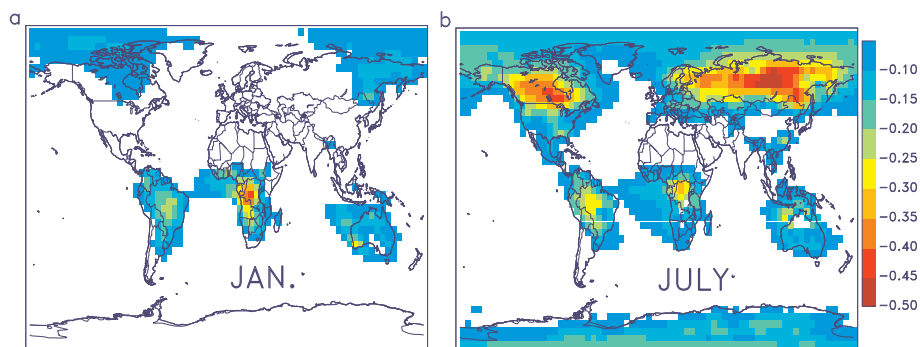


Figure S9: **Calculated change in precipitation pH due to the additional secondary biogenic source of HCOOH inferred from IASI data (Opt2).** **a**, In January. **b**, In July.

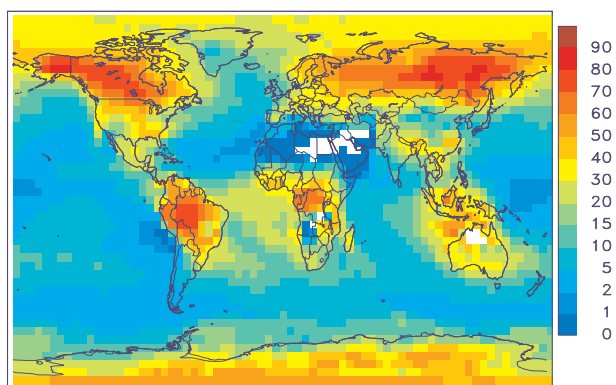


Figure S10: **Calculated contribution (%) of HCOOH to the total concentration of hydrogen cations  $[H^+]$ .** Results are from the Opt2 source inversion in July.

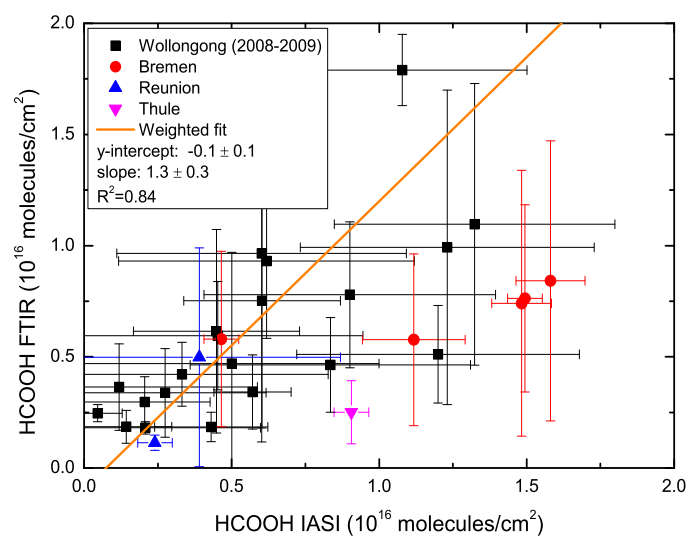


Figure S11: **Comparison between IASI columns and FTIR measurements at different sites.** FTIR data at Wollongong and Reunion Island are presented in this study, at Thule (2004-2008) and Bremen (2002-2010) are obtained from Ref. [S7]. The regression line applies to Wollongong and Reunion Island data.



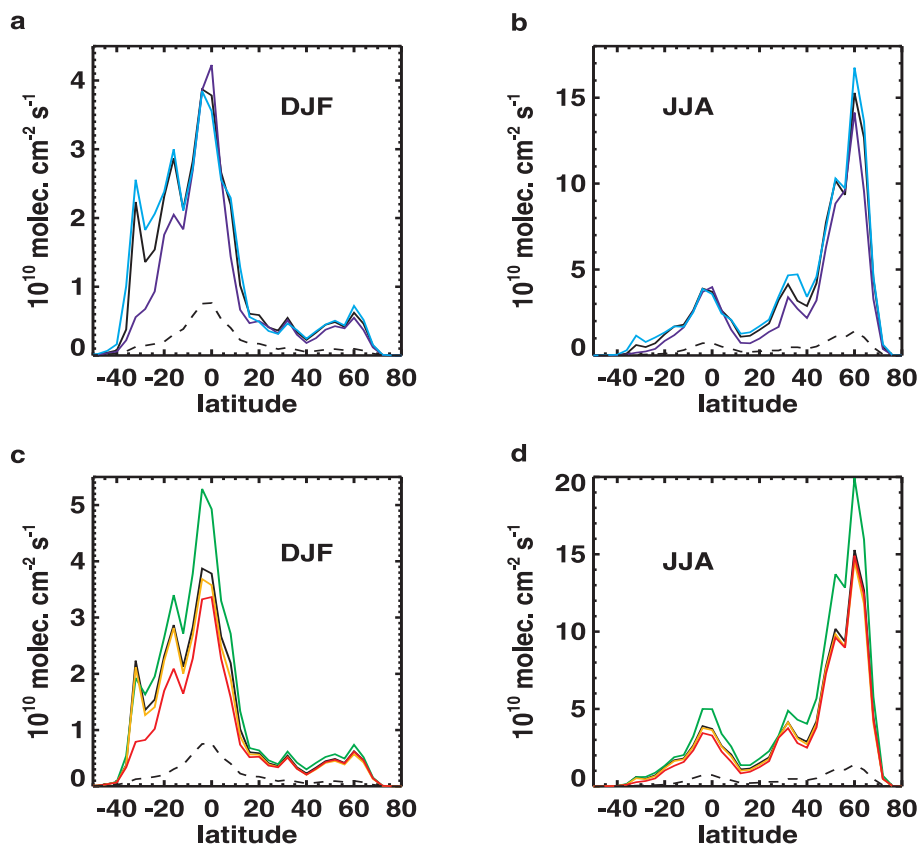


Figure S12: Latitudinal profiles of “top-down” biogenic emissions of the HCOOH precursor averaged over December-January-February (DJF) and June-July-August (JJA). **a-b**, Opt2 in black, Opt2-Err:2 in light blue, Opt2-Errx2 in dark blue. **c-d**, Opt2 in black, Opt1 in green, Opt2-kOH in orange, Opt2-Isom in red. The dashed lines represent the a priori distribution of the HCOOH precursor used in the optimisations. The other sensitivity inversions lie very close to the standard Opt2 results and are not illustrated here.

## References

- [S1] Müller, J.-F. & Stavrakou, T. Inversion of CO and NO<sub>x</sub> emissions using the adjoint of the IMAGES model. *Atmos. Chem. Phys.* **5**, 1157–1186 (2005).
- [S2] Stavrakou, T., Müller, J.-F., Boersma, F., De Smedt, I. & van der A, R. Assessing the distribution and growth rates of NO<sub>x</sub> emission sources by inverting a 10-year record of NO<sub>2</sub> satellite columns. *Geophys. Res. Lett.* **35**, L10810, doi:10.1029/2008GL033521 (2008).
- [S3] Stavrakou, T. *et al.* Evaluating the performance of pyrogenic and biogenic emission inventories against one decade of space-based formaldehyde columns. *Atmos. Chem. Phys.* **9**, 1037–1060 (2009).
- [S4] Stavrakou, T., Peeters, J. & Müller, J.-F. Improved global modelling of HO<sub>x</sub> recycling in isoprene oxidation : evaluation against the GABRIEL and INTEX-A aircraft campaign measurements. *Atmos. Chem. Phys.* **10**, 9863–9878 (2010).
- [S5] Schultz, M. G. *et al.* Global wildland fire emissions from 1960 to 2000. *Global Biogeochem. Cy.* **22**, GB2002, doi:10.1029/2007GB003031 (2008).
- [S6] Ohara, T. *et al.* An Asian emission inventory of anthropogenic emission sources for the period 1980–2020. *Atmos. Chem. Phys.* **7**, 4419–4444 (2007).
- [S7] Paulot, F. *et al.* Importance of secondary sources in the atmospheric budgets of formic and acetic acids. *Atmos. Chem. Phys.* **11**, 1989–2013 (2011).
- [S8] Guenther, A. *et al.* Estimates of global terrestrial isoprene emissions using MEGAN (Model of Emissions of Gases and Aerosols from Nature). *Atmos. Chem. Phys.* **6**, 3181–3210 (2006).
- [S9] van der Werf, G. R. *et al.* Global fire emissions and the contribution of deforestation, savanna, forest, agricultural, and peat fires (1997–2009). *Atmos. Chem. Phys.* **10**, 11,707–11,735 (2010).
- [S10] Andreae, M. O. & Merlet, P. Emission of trace gases and aerosols from biomass burning. *Global Biogeochem. Cy.* **15**, 955–966 (2001).
- [S11] Lathière, J. *et al.* Impact of climate variability and land use changes on global biogenic volatile organic compound emissions. *Atmos. Chem. Phys.* **6**, 2129–2146 (2006).
- [S12] Peeters, J., Nguyen, T. L. & Vereecken, L. HO<sub>x</sub> radical regeneration in the oxidation of isoprene. *Phys. Chem. Chem. Phys.* **11**, 5935–5939 (2009).
- [S13] Peeters, J. & Müller, J.-F. HO<sub>x</sub> radical regeneration in isoprene oxidation via peroxy radical isomerisations, II: Experimental evidence and global impact. *Phys. Chem. Chem. Phys.* **12**, 14,227–14,235 (2010).

- 496 [S14] Lelieveld, J. *et al.* Atmospheric oxidation capacity sustained by a tropical  
497 forest. *Nature* **452**, 737–740 (2008).
- 498 [S15] Martinez, M. *et al.* Hydroxyl radicals in the tropical troposphere over  
499 the Suriname rainforest: airborne measurements. *Atmos. Chem. Phys.* **10**,  
500 3759–3773 (2010).
- 501 [S16] Paulot, F. *et al.* Unexpected epoxide formation in the gas-phase photoox-  
502 idation of isoprene. *Science* **325**, 730–733 (2009).
- 503 [S17] Archibald, A. T. *et al.* Impacts of mechanistic changes on HOx formation  
504 and recycling in the oxidation of isoprene. *Atmos. Chem. Phys.* **10**, 8097–8118  
505 (2010).
- 506 [S18] Paulot, F. *et al.* Isoprene photooxidation: new insights into the production  
507 of acids and organic nitrates. *Atmos. Chem. Phys.* **9**, 1479–1501 (2009).
- 508 [S19] Butkovskaya, N. I., Pouvesle, N., Kukui, A. & Le Bras, G. Mechanism  
509 of the OH-initiated oxidation of glycolaldehyde over the temperature range  
510 233–296 K. *J. Phys. Chem. A* **110**, 13,492–13,499 (2006).
- 511 [S20] Saunders, S.M., Jenkin, M. E., Derwent, R. G. & Pilling, M. J. Protocol  
512 for the development of the Master Chemical Mechanism, MCM v3 (Part A):  
513 tropospheric degradation of non-aromatic volatile organic compounds. *Atmos.*  
514 *Chem. Phys.* **3**, 161–180 (2003).
- 515 [S21] Butkovskaya, N. I., Pouvesle, N., Kukui, A., Mu, Y. & Le Bras, G. Mech-  
516 anism of the OH-initiated oxidation of hydroxyacetone over the temperature  
517 range 236–298 K. *J. Phys. Chem. A* **110**, 6833–6843 (2006).
- 518 [S22] Orlando, J. J. & Tyndall, G. S. Mechanism for the oxidation of hydrox-  
519 yacetone under atmospheric conditions. *AGU Fall Meeting, Abstract A11F-*  
520 *0115* (2010).
- 521 [S23] Atkinson, R. Gas-phase tropospheric chemistry of volatile organic com-  
522 pounds: 1. Alkanes and alkenes. *J. Phys. Chem. Ref. Data* **26**, 215–290  
523 (1997).
- 524 [S24] Neeb, P., Sauer, F., Horie, O. & Moortgat, G. K. Formation of hydrox-  
525 ymethyl hydroperoxide and formic acid in alkene ozonolysis in the presence  
526 of water vapour. *Atmos. Environ.* **31**(10), 1417–1423 (1997).
- 527 [S25] Atkinson, R. *et al.* Evaluated kinetic and photochemical data for atmo-  
528 spheric chemistry: Volume II - gas phase reactions of organic species. *Atmos.*  
529 *Chem. Phys.* **6**, 3625–4055 (2006).
- 530 [S26] Hatakeyama, S. & Akimoto, H. Reactions of Criegee intermediates in the  
531 gas phase. *Res. Chem. Intermed.* **20**, 503–524 (1994).

- [S27] Horie, O., Neeb, P., Limbach S. & Moortgat G. K. Formation of formic acid and organic peroxides in the ozonolysis of ethene with added water vapour. *Geophys. Res. Lett.* **21**, 1523–1526 (1994).
- [S28] Hasson, A. S., Orzechowska, G. E. & Paulson, S. E. Production of stabilized Criegee intermediates and peroxides in the gas phase ozonolysis of alkenes 1. Ethene, trans-2-butene, and 2,3-dimethyl-2-butene. *J. Geophys. Res.* **106**, 34,131–34,142 (2001).
- [S29] Leather, K. E. *et al.* Acid-yield measurements of the gas-phase ozonolysis of ethene as a function of humidity using Chemical Ionisation Mass Spectrometry (CIMS). *Atmos. Chem. Phys. Discuss.* **11**, 25173–25204, 2011.
- [S30] Ryzhkov, A. B. & Ariya, P. A. A theoretical study of the reactions of parent and substituted Criegee intermediates with water and the water dimer. *Phys. Chem. Chem. Phys.* **6**, 5042–5050 (2004).
- [S31] Hasson, A. S., Ho, A. W., Kuwata, K. T. & Paulson, S. E. Production of stabilized Criegee intermediates and peroxides in the gas phase ozonolysis of alkenes 2. Asymmetric and biogenic alkenes. *J. Geophys. Res.* **106**, 34,143–34,153 (2001).
- [S32] Lee, J. H., Leahy, D. F., Tang, I. N. & Newman, L. Measurement and speciation of gas phase peroxides in the atmosphere. *J. Geophys. Res.* **98**, 2911–2915 (1993).
- [S33] Weinstein-Lloyd, J. B. *et al.* Measurements of peroxides and related species during the 1995 summer intensive of the Southern Oxidants Study in Nashville, Tennessee. *J. Geophys. Res.* **103**, 22,361–22,373 (1998).
- [S34] Sauer, F., Beck, J., Schuster, G., & Moortgat, G. K. Hydrogen peroxide, organic peroxides and organic acids in a forested area during FIELDVOC'94. *Chemosphere - Global Change Science* **3**, 309–326 (2001).
- [S35] Valverde-Canossa, J. *et al.* First measurements of H<sub>2</sub>O<sub>2</sub> and organic peroxides surface fluxes by the relaxed eddy-accumulation technique. *Atmos. Environ.* **40**, S55–S67 (2006).
- [S36] Bauerle, S. & Moortgat, G. K. Absorption cross-sections of HOCH<sub>2</sub>OOH vapor between 205 and 360 nm at 298 K. *Chem. Phys. Lett.* **309**, 43–48 (1999).
- [S37] Francisco, J. S. & Eisfeld, W. Atmospheric oxidation mechanism of hydroxymethyl hydroperoxide. *J. Phys. Chem. A* **113**, 7593–7600 (2009).
- [S38] Veyret, B. *et al.* Kinetics and mechanism of the photooxidation of formaldehyde. 1. Flash photolysis study. *J. Phys. Chem.* **93**, 2368–2374 (1989).

- [S39] Hermans, I., Müller, J.-F., Nguyen, T. L., Jacobs, P. A. & Peeters, J. Kinetics of  $\alpha$ -hydroxy-alkylperoxyl radicals in oxidation processes.  $\text{HO}_2$ -initiated oxidation of ketones/aldehydes near the tropopause. *J. Phys. Chem. A* **109**, 4303–4311 (2005).
- [S40] Vereecken, L., Nguyen, T. L., & Peeters, J. Computational study of the stability of  $\alpha$ -hydroperoxyl- or  $\alpha$ -alkylperoxyl substituted alkyl radicals. *Chem. Phys. Lett.* **393**, 432–436, 2004.
- [S41] O’Sullivan, D. W., Lee, M., Noone, B. C. & Heikes, B. G. Henry’s law constant determinations for hydrogen peroxide, methyl hydroperoxide, hydroxymethyl hydroperoxide, ethyl hydroperoxide, and peroxyacetic acid. *J. Phys. Chem.* **100**, 3241–3247 (1996).
- [S42] Chen, Z. M. *et al.* Aqueous-phase ozonolysis of methacrolein and methyl vinyl ketone: a potentially important source of atmospheric aqueous oxidants. *Atmos. Chem. Phys.* **8**, 2255–2265 (2008).
- [S43] Nguyen, T. L., Peeters, J. & Vereecken, L. Theoretical study of the gas-phase ozonolysis of  $\beta$ -pinene ( $\text{C}_{10}\text{H}_{16}$ ). *Phys. Chem. Chem. Phys.* **11**, 5643–5656 (2009).
- [S44] Orlando, J. J. *et al.* Product studies of the OH- and ozone-initiated oxidation of some monoterpenes. *J. Geophys. Res.* **105** (D9), 11,561–11,572, doi:10.1029/2000JD900005 (2000).
- [S45] Fantechi, G. *Atmospheric oxidation reactions of selected biogenic volatile organic compounds (BIOVOCs): A smog chamber study*. (Ph.D. Thesis, University of Leuven, 1999).
- [S46] Lee, A. *et al.* Gas-phase products and secondary aerosol yields from the ozonolysis of ten different terpenes. *J. Geophys. Res.* **111**, D07302, doi:10.1029/2005JD006437 (2006).
- [S47] Larsen, B. R. *et al.* Gas-Phase OH Oxidation of Monoterpenes: Gaseous and Particulate Products. *J. Atmos. Chem.* **38**, 231–276 (2001).
- [S48] Zhang, P., Anderson, M., Barlow, B., Tan, B., & Myneni, R. B. Climate-related vegetation characteristics derived from Moderate Resolution Imaging Spectroradiometer (MODIS) leaf area index and normalized difference vegetation index. *J. Geophys. Res.* **109**, D20105, doi:10.1029/2004JD004720 (2004).
- [S49] Stavrakou, T. *et al.* The continental source of glyoxal estimated by the synergistic use of spaceborne measurements and inverse modelling. *Atmos. Chem. Phys.* **9**, 8431–8446 (2009b).
- [S50] Sellegri, K. *et al.* Contribution of gaseous and particulate species to droplet solute composition at the Puy de Dôme, France. *Atmos. Chem. Phys.* **3**, 1509–1522 (2003).

- 607 [S51] Chameides, W. L. The photochemistry of a remote marine stratiform  
608 cloud. *J. Geophys. Res.* **89**, 4739–4755 (1984).
- 609 [S52] Crowley, J. N. Evaluated kinetic and photochemical data for atmospheric  
610 chemistry: Volume V - heterogeneous reactions on solid substrates. *Atmos.*  
611 *Chem. Phys.* **10**, 9059–9223 (2010).
- 612 [S53] Heymsfield, A. J. & McFarquhar, G. M. High albedos of cirrus in the  
613 tropical pacific warm pool: Microphysical interpretations from CEPEX and  
614 from Kwajalein, Marshall Islands. *J. Atmos. Sci.* **53**, 2424–2451 (1996).
- 615 [S54] Schmitt, C. G. & Heymsfield, A. J. Total surface area estimates for in-  
616 dividual ice particles and particle populations. *J. App. Met.* **44**, 467–474  
617 (2005).
- 618 [S55] Bond, T. *et al.* A technology-based global inventory of black  
619 and organic carbon emissions from combustion. *J. Geophys. Res.* **109**,  
620 doi:10.1029/2003JD003697 (2004).
- 621 [S56] Martin, R. V. *et al.* Global and regional decreases in tropospheric ox-  
622 idants from photochemical effects of aerosols. *J. Geophys. Res.* **108**, 4097,  
623 doi:10.1029/2002JD002622 (2003).
- 624 [S57] Henze, D. K. *et al.* Global modeling of secondary organic aerosol formation  
625 from aromatic hydrocarbons: high- vs. low-yield pathways. *Atmos. Chem.*  
626 *Phys.* **8**, 2405–2421 (2008).
- 627 [S58] Chang, E. I. & Pankow, J. F. Organic particulate matter formation at  
628 varying relative humidity using surrogate secondary and primary organic  
629 compounds with activity corrections in the condensed phase obtained using  
630 a method based on the Wilson equation. *Atmos. Chem. Phys.* **10**, 5475–5490  
631 (2010).
- 632 [S59] Henze, D. K. & Seinfeld, J. H. Global secondary organic aerosol from iso-  
633 prene oxidation. *Geophys. Res. Lett.* **33**, L09812, doi:10.1029/2006GL025976  
634 (2006).
- 635 [S60] Ceulemans, K., Müller, J.-F. & Compernelle, S. Parameterising secondary  
636 organic aerosol from  $\alpha$ -pinene using a detailed oxidation and aerosol formation  
637 model. *Atmos. Chem. Phys. Discuss.*, submitted (2011).
- 638 [S61] Capouet, M., Müller, J.-F., Ceulemans, K., Compernelle, S., Vereecken,  
639 L. & Peeters, J. Modeling aerosol formation in  $\alpha$ -pinene photooxidation ex-  
640 periments. *J. Geophys. Res.* **113**, doi:10.1029/2007JD008995 (2008).
- 641 [S62] Ceulemans, K., Compernelle, S., Peeters, J., & Muller, J.-F.. Evaluation  
642 of a detailed model of secondary organic aerosol formation from  $\alpha$ -pinene  
643 against dark ozonolysis experiments. *Atmos. Environ.* **40**, 5434–5442 (2010).

- [S63] Fu, T.-M. *et al.* Global budgets of atmospheric glyoxal and methylglyoxal, and implications for formation of secondary organic aerosols. *J. Geophys. Res.* **113**, doi:10.1029/2007JD009505 (2008).
- [S64] Spracklen, D. V. *et al.* Aerosol mass spectrometer constraint on the global secondary organic aerosol budget. *Atmos. Chem. Phys. Discuss.* **11**, 5699–5755 (2011).
- [S65] Malm, W. C., Schichtel, B. A., Pitchford, M. L., Ashbaugh, L. L., & Eldred, R. A. Spatial and monthly trends in speciated fine particle concentration in the United States. *J. Geophys. Res.* **109**, D03306, doi:10.1029/2003JD003739 (2004).
- [S66] Yttri, K. E. *et al.* Elemental and organic carbon in PM10: a one year measurement campaign within the European Monitoring and Evaluation Programme EMEP. *Atmos. Chem. Phys.* **7**, 5711–5725 (2007).
- [S67] Perrin, A. & Vander Auwera, J. An improved database for the 9 micron region of the formic acid spectrum. *J. Quant. Spectrosc. Radiat. Transfer* **108**, 363–370 (2007).
- [S68] Rothman, L. S. *et al.* The HITRAN 2008 molecular spectroscopy database. *J. Quant. Spectrosc. Radiat. Transfer* **110**, 533–572 (2009).
- [S69] Emmons, L. K. *et al.* Data composites of airborne observations of tropospheric ozone and its precursors. *J. Geophys. Res.* **105**, 20,497–20,538 (2000).
- [S70] Singh, H. B., Thompson, A. M. & Schlager, H. SONEX airborne mission and coordinated POLINAT-2 activity: Overview and accomplishments. *Geophys. Res. Lett.* **26**, 3053–3056 (1999).
- [S71] Singh, H. B., Brune, W. H., Crawford, J. H., Flocke, F. & Jacob, D. J. Chemistry and transport of pollution over the Gulf of Mexico and the Pacific: spring 2006 INTEX-B campaign overview and first results. *Atmos. Chem. Phys.* **9**, 2301–2318 (2009).
- [S72] Karl, T. *et al.* Efficient Atmospheric cleansing of oxidized organic trace gases by vegetation. *Science* **330**, 816–819, doi: 10.1126/science.1192534 (2010).
- [S73] Kalnay, E. *et al.* The NCEP/NCAR 40-year reanalysis project, *Bull. Amer. Meteor. Soc.* **77**, 437–470 (1996).
- [S74] Galano, A., Alvarez-Idaboy, J. R., Ruiz-Santoyo, M. E. & Vivier-Bunge, A. Rate coefficient and mechanism of the gas phase OH hydrogen abstraction reaction from formic acid: A quantum mechanical approach. *J. Phys. Chem. A* **106**, 9520–9528 (2002).
- [S75] Turquety, S. *et al.* Inventory of boreal fire emissions for North America in 2004: Importance of peat burning and pyroconvective injection, *J. Geophys. Res.* **112**, D12S03, doi:10.1029/2006JD007281 (2007).

- [S76] Dentener, F. *et al.* Emissions of primary aerosol and precursor gases in the years 2000 and 1750 prescribed data-sets for AeroCom. *Atmos. Chem. Phys.* **6**, 4321–4344 (2006).
- [S77] Johnson, B. J. & Dawson G. A. A preliminary study of the carbon-isotopic content of ambient formic acid and two selected sources : automobile exhaust and formicine ants. *J. Atmos. Chem.* **17**, 123–140 (1993).
- [S78] Villanueva-Fierro, I., Popp, C. J. & Martin, R. S. Biogenic emissions and ambient concentrations of hydrocarbons, carbonyl compounds and organic acids from ponderosa pine and cottonwood trees at rural and forested sites in Central New Mexico. *Atmos. Environ.* **38**, 249–260 (2004).
- [S79] Martin, R. S. *et al.* Measurement of isoprene and its atmospheric oxidation products in a Central Pennsylvania deciduous forest. *J. Atmos. Chem.* **13**, 1–92 (1991).
- [S80] Andreae, M. O., R. W. Talbot & Li, S.-M. Atmospheric Measurements of Pyruvic and Formic Acid. *J. Geophys. Res.* **92(D6)**, 6635–6641 (1987).
- [S81] Talbot, R. W. *et al.* Carboxylic acids in the rural continental atmosphere over the eastern United States during the Shenandoah Cloud and Photochemistry Experiment. *J. Geophys. Res.* **100(D5)**, 9335–9343 (1995).
- [S82] Talbot, R., Beecher, K., Harriss, R. & Cofer W. III : Atmospheric geochemistry of formic and acetic acids at a mid-latitude temperate site. *J. Geophys. Res.* **93(D2)**, 1638–1652 (1988).
- [S83] Sanhueza, E. & Andreae, M. O. Emissions of formic and acetic acids from tropical savanna soils. *Geophys. Res. Lett.* **18(9)**, 1707–1710 (1991).
- [S84] Sanhueza, E., Figueroa, L. & Santana, M. Atmospheric formic and acetic acids in Venezuela. *Atmos. Environ.* **30**, 1861–1873 (1996a).
- [S85] Sanhueza, E., Santana, M. & Hermoso, M. Gas- and aqueous- phase formic and acetic acids at a tropical cloud forest site. *Atmos. Environ.* **26**, 1421–1426 (1992).
- [S86] Karl, T. *et al.* Exchange processes of volatile organic compounds above a tropical rain forest: Implications for modelling tropospheric chemistry above dense vegetation. *J. Geophys. Res.* **109**, D18306, doi:10.1029/2004JD004738 (2004).
- [S87] Andreae, M. O., Talbot, R. W., Andreae, T. W. & and Harriss, R. C. Formic and Acetic Acid Over the Central Amazon Region, Brazil 1. Dry Season. *J. Geophys. Res.* **93(D2)**, 1616–1624 (1988).
- [S88] Kesselmeier, J. *et al.* Concentrations and species composition of atmospheric volatile organic compounds (VOCs) as observed during the wet and dry season in Rondônia (Amazonia). *J. Geophys. Res.* **107(D20)**, 8053, doi:10.1029/2000JD000267 (2002).



- 722 [S89] Talbot, R. W., Andreae, M. O., Berresheim, H., Jacob, D. J. & Beecher,  
723 K. M. Sources and sinks of formic, acetic and pyruvic acids over Central  
724 Amazonia, 2. Wet season. *J. Geophys. Res.* **95(D10)**, 16,799–16,811 (1990).
- 725 [S90] Puxbaum, H. *et al.* Atmospheric concentrations of formic and acetic  
726 acid and related compounds in eastern and northern Austria. *Atmos. En-*  
727 *viron.* **22(12)**, 2841–2850 (1988).
- 728 [S91] Helas, G., Bingemer, H. & Andreae, M. O. Organic acids over Equatorial  
729 Africa : Results from DECAFE 88. *J. Geophys. Res.* **97(D6)**, 6187–6193  
730 (1992).
- 731 [S92] Servant, J., Kouadio, G., Cros, B. & Delmas, R. Carboxylic Monoacids  
732 in the air of Mayombe forest (Congo) : Role of the forest as a source or sink.  
733 *J. Atmos. Chem.* **12**, 367–380 (1991).
- 734 [S93] Kumar, N. *et al.* Measurements of formic and acetic acid levels in the  
735 vapour phase at Dayalbagh, Agra, India. *Atmos. Environ.* **20**, 3545–3550  
736 (1996).
- 737 [S94] Khare, P., Sastangi, G. S., Kumar, N., Kumari, K. M. & Srivastava, S. S.  
738 HCHO, HCOOH and CH<sub>3</sub>COOH in air and rain water at a rural tropical site  
739 in North Central India. *Atmos. Environ.* **31**, 3867–3875 (1997).
- 740 [S95] Keene, W. C. & Galloway, J. N. Organic acidity of precipitation of North  
741 America. *Atmos. Environ.* **18**, 2491–2497 (1984).
- 742 [S96] Schaefer, D. A., Lindberg, S. E. & Hoffman, W. A. Fluxes of undissociated  
743 acids to terrestrial ecosystems by atmospheric deposition. *Tellus* **41B**, 207–  
744 218 (1989).
- 745 [S97] Brooks Avery, G. Jr., Yang, Y., Kieber, R. J. & Willey, J. D. Impact of  
746 recent urbanization on formic and acetic acid concentrations in coastal North  
747 Carolina rainwater. *Atmos. Environ.* **35**, 3353–3359 (2001).
- 748 [S98] Sakugawa, H., Kaplan, I. R. & Shepard, L. S. Measurements of H<sub>2</sub>O<sub>2</sub>,  
749 aldehydes, and organic acids in Los Angeles rainwater: their sources and  
750 deposition rates. *Atmos. Environ.* **27B**, 203–219 (1993).
- 751 [S99] Sanhueza, E. *et al.* Field measurement evidence for an atmospheric chem-  
752 ical source of formic and acetic acids in the tropic. *Geophys. Res. Lett.* **23(9)**,  
753 1045–1048 (1996b).
- 754 [S100] Sanhueza, E., Alfonzo, Y. & Santana, M. Compuestos orgánicos volátiles  
755 en la atmósfera de la Gran Sabana. II: HCHO, HCOOH y CH<sub>3</sub>COOH en  
756 lluvias. *Interciencia* **28(1)**, 29–35 (2003).
- 757 [S101] Sanhueza, E., Donoso, L., Santana, M., Fernández, E. & Romero, J.  
758 Atmospheric chemistry over the Auyantepuy (5° 46' N; 62° 30' W; 2100  
759 meters a.s.l.). *Interciencia* **24**, 372–380 (1999).

- [S102] Andreae, M., Talbot, R., Berresheim, H. & Beecher, K. Precipitation Chemistry in Central Amazonia. *J. Geophys. Res.* **95(D10)**, 16,987–16,999 (1990).
- [S103] Pauliquevis, T., Lara, L. L., Antunes, M. L. & Artaxo, P. Aerosol and precipitation chemistry in a remote site in Central Amazonia : The role of biogenic contribution. *Atmos. Chem. Phys. Discuss.* **7**, 11,465–11,509 (2007).
- [S104] Yoboué, Y., Galy-Lacaux, C., Lacaux, J. P. & Silué, S. Rainwater chemistry and wet deposition over the wet savanna ecosystem of Lamto (Côte d’Ivoire). *J. Atmos. Chem.* **52**, 117–141 (2005).
- [S105] Williams, R. M., Fisher, T. R. & Melack, J. M. Chemical composition and deposition of rain in the Central Amazon, Brazil. *Atmos. Environ.* **31**, 207–217 (1997).
- [S106] Zunckel, M., Saizar, C. & Zarauz, J. Rainwater composition in northeast Uruguay. *Atmos. Environ.* **37**, 1601–1611 (2003).
- [S107] Galloway, J. N., Keene, W. C. & Likens, G. E. Processes controlling the composition at a remote southern hemispheric location : Torres del Paine National Park, Chile. *J. Geophys. Res.* **101(D3)**, 6883–6897 (1996).
- [S108] Galy-Lacaux, C. & Modi, A. I. Precipitation chemistry in the Sahelian savanna of Niger, Africa. *J. Atmos. Chem.* **30**, 319–343 (1998).
- [S109] Mphepya, J. N., Pienaar, J. J., Galy-Lacaux, C., Held, G. & Turner, C. R. Precipitation chemistry in semi-arid areas of Southern Africa : a case study for a rural and an industrial site. *J. Atmos. Chem.* **47**, 1–24 (2004).
- [S110] Sigha-Nkamdjou, L. *et al.* Rainwater chemistry and wet deposition over the Equatorial forested ecosystem of Zoétélé (Cameroon). *J. Atmos. Chem.* **46**, 173–198 (2003).
- [S111] Lacaux, J. P., Delmas, R., Kouadio, G., Cros, B. & Andreae, M. O. Precipitation chemistry in the Mayombe Forest of Equatorial Africa. *J. Geophys. Res.* **97(D6)**, 6195–6206 (1992).
- [S112] Durana, N. *et al.* Organic acids in precipitation in the Basque Country (North of Spain), *Atmos. Res.* **28**, 93–101 (1992).
- [S113] Glasius, M. *et al.* Relative contribution of biogenic and anthropogenic sources to formic and acetic acids in the atmospheric boundary layer. *J. Geophys. Res.* **106(D7)**, 7415–7426 (2001).
- [S114] Peña, R. M. *et al.* Organic acids and aldehydes in rainwater in a north-west region of Spain. *Atmos. Environ.* **36**, 5277–5288 (2002).
- [S115] Moschonas, N. & Glavas, S. Weak organic acidity in a wet-only precipitation study at a Mediterranean coastal site, Patras, Greece. *Atmos. Res.* **63**, 147–157 (2002).

- 798 [S116] Galloway, J. N. & Gaudry, A. The composition of precipitation on Am-  
799 sterdam Island, Indian Ocean. *Atmos. Environ.* **18**, 2649–2656 (1984).
- 800 [S117] Post, D., Bridgman, H. A. & Ayers, G. P. Fog and rainwater composition  
801 in rural SE Australia. *J. Atmos. Chem.* **13**, 83–95 (1991).
- 802 [S118] Likens, G. E., Keene, W. C., Miller, J. M. & Galloway, J. N. Chem-  
803 istry of precipitation from a remote terrestrial site in Australia. *J. Geophys.*  
804 *Res.* **92(D11)**, 13,299–13,314 (1987).
- 805 [S119] Ayers, G. P., Gillett, R. W. & Selleck, P. A pilot study on rain-water  
806 composition at Darwin Airport. *Aust. Met. Mag.* **42**, 143–150 (1993).
- 807 [S120] Zhang, Y.-L., Lee, X.-Q., Huang, D.-K., Huang, R.-S. & Jiang, W.  
808 Low molecular weight carboxylic acids in precipitation during the rainy  
809 season in the rural area of Anshun, West Guizhou province. *Huanjing*  
810 *Kexue/Environmental Science*, **30(3)**, 644–649 (2009).
- 811 [S121] Keene, W. C. *et al.* Processes controlling variability in the chemical com-  
812 position of precipitation at a remote, temperate site in south-central China,  
813 Fourth Scientific Advisory Council, International Geosphere-Biosphere Pro-  
814 gramme, Beijing (1995).
- 815 [S122] Singh, S. P. *et al.* Rainwater composition at a regional representative  
816 site of semi-arid region of India. *Water, Air, and Soil Pollution* **127**, 93–108  
817 (2001).